ELSEVIER

Contents lists available at ScienceDirect

International Journal of Heat and Mass Transfer

journal homepage: www.elsevier.com/locate/ijhmt





Effect of evolving recirculation zones on anomalous solute transport in rough single fractures

Kun Xing^a, Xiaoqing Shi^{a,*}, Peter K. Kang^b, Xueyuan Kang^{a,*}, Jiazhong Qian^c, Lei Ma^c, Jichun Wu^a

- a Key Laboratory of Surficial Geochemistry of Ministry of Education, School of Earth Sciences and Engineering, Nanjing University, Nanjing 210023, China
- ^b Department of Earth and Environmental Sciences, University of Minnesota, Minneapolis, MN 55455, USA
- ^c School of Resources and Environmental Engineering, Hefei University of Technology, Hefei 230009, China

ARTICLE INFO

Keywords: Recirculation zones Mass transfer Anomalous transport Rough single fractures

ABSTRACT

Understanding the anomalous solute transport in single fractures is important for many hydrogeologic processes and subsurface applications. Recirculation zones (RZs) and corresponding main flow zones (MFZs) have been widely recognized as low-velocity regions and preferential pathways that could explain the simple anomalous solute transport, i.e., heavy tailings and early arrival. However, the direct relation between RZs and more complex anomalous transport phenomena, e.g., multi-modal peaks and fluctuating tailings, has been elusive. This may be due to the limited understanding of the evolution of RZs and the mass transfer process between RZs and MFZs, i.e., the monotonically increasing RZs volume (S_{ν}) and defaulted diffusion-dominated mass transfer. In this study, we systematically generate a series of 2D/3D rough single fractures with different geometric properties to investigate the evolution of RZs and its influence on anomalous transport across a wide Re range of 0-426.88. Three-stage evolution of RZs with increasing Re was identified by using the growth rate of S_V (dS_V/dRe), the rapid growth stage (Stage I) where dS_{ν}/dRe increase, the slow growth stage (Stage II) where dS_{ν}/dRe decrease, and the fully developed stage (Stage III) where dS_{ν}/dRe is a constant. The mass transfer mode between recirculation and main flow zones is shifted from diffusion-dominated in $Stage\ I$ to convection-dominated in $Stage\ II$ due to the enhanced convection in RZs. This shift of mass transfer mode enhances the mass transfer rate (α) between RZs and MFZs by 5-20 times. In Stage II, the solute was trapped around the interface between RZs and MFZs before entering RZs, i.e., the solute "film". The coexistence of the solute "film" and the solutes trapped by RZs induces multi-modal peaks and strengthened tailings of BTCs. In Stage III, the solute "film" cannot form due to the rapid dissipation of detained solutes driven by stronger convection-dominated mass transfer around the RZs-MFZs interface, which in turn leads to the disappearance of multi-modal peaks and induces monotonically shortened tailings. This study fills the gap in the RZs evolution and the associated mass transfer process in the microscopic flow fields, which deepens our understanding of the anomalous transport mechanism.

1. Introduction

A better understanding of solute transport in fractures is critical for many hydrogeological processes and engineering applications [1–5]. Initially, a single fracture was idealized as two smooth parallel plates [3]. Due to the two smooth parallel plates being statistically homogeneous and stationary, solute transport in the idealized fracture is commonly assumed to follow Fick's law, where the dispersion coefficient is spatially and temporally constant [6,7] and the traditional advection-dispersion equation (ADE) holds true [8,9,10].

However, the single fractures in nature are highly heterogeneous due to their rough fracture wall surfaces and tortuosity [1,8,11]. Therefore, solute transport processes in rough single fractures that do not conform to Fick's law are often observed [11–13]. The corresponding breakthrough curves (BTCs) exhibit typical anomalous (non-Fickian) characteristics, i.e., the early arrival and heavy tailing of breakthrough curves (BTCs), such behaviors are referred to as anomalous solute transport [1,9,12].

Much effort has been devoted to investigating the mechanisms of anomalous solute transport in rough single fractures. The widely

E-mail addresses: shixq@nju.edu.cn (X. Shi), xykang@smail.nju.edu.cn (X. Kang).

^{*} Corresponding authors.

accepted mechanisms of anomalous transport can be attributed to two underlying mechanisms, both relate to local flow field heterogeneity: (1) the limited spatial and temporal scales to make solute transport not yet reach a Fickian state [8,13,14]; (2) incomplete local mixing resulting from a complex flow field takes place, for example, the preferential flow [15–17]. Even though the effect of heterogeneity (e.g., roughness, variance, and correlation length of fracture aperture field) on the flow field has been extensively investigated for decades, the impact of microscopic heterogeneity on anomalous transport is still a hot issue [13].

Numerous studies have shown the critical role of recirculation zones (RZs), which were widely detected in the microscopic flow field, in controlling the early arrival and heavy tailing [18–21]. Physically the RZs form near the rough fracture walls when the fluid flows through due to the abrupt change in aperture space [19,22,23]. The formation of RZs causes a faster flow speed through the central channel (or the main flow zones (MFZs)). Solute remains in the MFZs breaking through quickly, but the solute that does enter the RZs resides there for longer.

However, the current understanding of the influence of RZs on anomalous transport cannot explain more complex anomalous transport phenomena detected in the field experiments and microfluidic experiments, e.g., the multi-modal peaks in effluent concentration [20,24,25] and the fluctuating tailings of the BTCs [25]. This is because the current understanding of RZs has the following limitations.

Firstly, the evolution of RZs in most previous studies is limited by a narrow Reynolds number (Re) range (Re = $\rho Vd/\mu$, ρ [kg/m³] is the fluid density, V [m/s] is flow velocity, d [m] is characteristic length, where d is the average aperture e_m , and μ is dynamic viscosity) [12,19,21,23, 26]. In previous studies, the monotonically increasing of RZs volume (S_{ν}) with increasing *Re* has been widely reported [23,26–28], which was considered as the main contribution to more solute trapping, resulting in heavier tailings [19,29]. Physically, the S_{ν} of a single RZ may not increase indefinitely with the continuously increasing Re due to the constraints of the limited void space and the main flow channels (MFZs). It can be expected that, if Re is large enough, the full evolution process of a RZ should go through several stages until S_{ν} is constant. The different evolution stages of RZs with increasing Re may induce different solute distributions. As Re increases, not only the S_v increases but also the internal kinetic energy within RZs [18,30]. The increase of internal kinetic energy may induce the change of flow dynamics within RZs, which in turn affects the solute distribution in the local flow field and induces the more complex anomalous transport. To date, the full evolution process of an RZ under a wide range of Re and associated impact on anomalous solute transport are rarely reported.

Secondly, few studies have directly investigated the mass transfer mode between RZs and MFZs, especially when it comes to high Re [30]. In most previous studies, the RZs and MFZs were assumed as two independent regions separated by the interface, the diffusion was the only transport mechanism between RZs and MFZs [19,21,26,30]. This assumption has also been adopted by some widely used models for anomalous solute transport, e.g., the mobile-immobile (MIM) model [12,25,30]. However, recent studies based on microfluid laboratory experiments and 3D simulations have observed the existence of direct convective mass flow between RZs and MFZs [18,31]. The convection-dominated mass transfer is fundamentally different from the diffusion-dominated mass transfer process, this may induce more complex anomalous phenomena that the existing MIM model cannot explain, e.g., the tailing shortening with increasing Re [31] and the multi-modal BTCs [18,20]. To date, there is no reasonable explanation for the different mass transfer modes (diffusion/convection) between RZs and MFZs and associated anomalous phenomena. Therefore, a systematic study on the RZs' evolution and corresponding mass transfer mode across a wide Re range is urgent to carry out to address the limitations of the current understanding of RZs.

To improve the current understanding of anomalous solute transport associated with RZs in rough single fractures, this study comprehensively

investigates the influence of RZs on anomalous solute transport across a wide *Re* range using high-resolution numerical simulations. This study elucidates the whole evolution process of RZs across a wide *Re* range and interprets the mechanism of the anomalous transport phenomena from the perspective of microscopic solute transport processes.

2. Methodologies

This study focused on the cases of flow and transport in a series of single two-dimensional (2D) fractures and a single three-dimensional (3D) fracture to achieve a balance between sufficient complexity and tractability while considering the dimensional impacts. The combination of 2D and 3D situations are ideal test cases and serve as an exploratory step for broadly understanding the mass transfer process in complex flow systems with RZs.

2.1. Governing equations

The Navier–Stokes equation governs fluid flow in rough single fractures:

$$\rho(\mathbf{u}\cdot\nabla)\mathbf{u} = \mu\nabla^2\mathbf{u} - \nabla P \tag{1}$$

$$\nabla \cdot \mathbf{u} = 0 \tag{2}$$

where **u** [m/s] is flow velocity; ρ [kg/m³] is fluid density; μ [Pa s] is dynamic fluid viscosity; and P [Pa] is the pressure.

The solute transport in rough fractures is governed by the advection-diffusion equation:

$$\frac{\partial C}{\partial t} = D(\nabla^2 C) - \nabla \cdot (\mathbf{u}C) \tag{3}$$

where D [m²/s] is the diffusion coefficient; C [mol/m³] is the concentration. In this study, NaCl is used as a conservative tracer.

In this study, the commercial finite element software of COMSOL Multiphysics® was employed to solve the Navier–Stokes equation and advection-diffusion equation.

2.2. Numerical experimental setup

2.2.1. Physical model setup

The geometry of natural rough fracture wall surfaces follows self-affine properties [2,21,26,32] and the height of fracture surfaces follows a power-law scaling [32–34]:

$$\lambda^H h(x) = h(\lambda x) \tag{4}$$

where h(x) is the equation describing the height of the fracture surface; λ [-] is a scaling factor; and the Hurst exponent H [-] represents different roughness ranging from 0 to 1 [35].

Generally, the Hurst exponent H of natural single fractures varies between 0.5 and 0.75 [36]. To obtain the physical models close to the natural fractures, H=0.5, 0.55, 0.60, 0.65, and 0.75 are chosen as the surface roughness parameters to generate the coordinate point sets of the upper and lower fracture wall surfaces. Following the numerical relationship between H and the fractal dimension D_f proposed by Develi and Babadagli [37], H is converted to D_f , which can be directly set in the Synfrac® software [38]. The point sets are then imported into COMSOL Multiphysics®. Using COMSOL's built-in parametric scanning module, five 2D rough single fractures (2D Fr-A, 2D Fr-B, 2D Fr-C, 2D Fr-D, and 2D Fr-E) are generated (shown in Fig. S1 in Support Information). The detailed process of constructing a physical fracture model using Synfrac® is shown in Text S1. All the geometric attributes of these 2D rough single fractures and definitions are listed in Table S1 and Text S2.

To consider the effect of dimensionality on the evolution process of RZs and the mass transfer between RZs and MFZs [31], 3D numerical simulations are also conducted in this study. The 3D physical model (3D

Fr-A) shown in Fig. 1(b) is obtained by extending the 2D physical model (2D Fr-A) in the z-direction (the extension length is 1 mm). Note that in both 2D and 3D simulations, the results are restricted to mass transfer in the fracture aperture field only, and the corresponding boundary conditions for the fracture walls are still set to be flux-free and do not consider the mass transfer in the matrix.

2.2.2. Boundary conditions and grid discretization

As shown in Fig. 1, the right boundary of fractures with x=100 served as the flow outlet with a constant pressure (i.e., $P_{-}out=0$ Pa). The left boundary of fracture with x=0 served as the flow inlet with a predefined pressure $P_{-}in$, $P_{-}in$ can be adjusted to the targeted fluid inertial effect quantified by Re. The fracture walls were assumed to be no-flux and no-slip boundaries.

The solute inlet (the left side of a single fracture) was set as an instantaneously released solute with a concentration of C_0 (1.0 mol/L), and the solute outlet (the right side of a single fracture) was set as an open boundary. The details of implementing instantaneous solute release in simulations are presented in Text S3. Other parameter settings for fracture flow and solute transport simulation are given in Appendixes A and B, respectively.

The length of 2D domains (2D Fr-A, 2D Fr-B, 2D Fr-C, 2D Fr-D, and 2D Fr-E) is 100 mm and the average aperture (e_m) of each fracture is given in Table S1, while the length and width of the 3D domain (3D Fr-A) is 100 mm and 1 mm, respectively, and e_m is 1.67 mm. To ensure that the simulation results are independent of the grid size, we performed a grid independence analysis in Fig. S2. As shown in Fig. S2, we used grids

with five different sizes to discretize the physical field, i.e., the conventional grid (\sim 2.56 \times 10⁻⁴ m), the refined grid (\sim 9.56 \times 10⁻⁵ m), the relatively refined grid (\sim 8.46 \times 10⁻⁵ m), hyperfine grid (\sim 7.46 \times 10⁻⁵ m), and extremely refined grid (\sim 3.46 \times 10⁻⁵ m). We compared the differences in the simulation results with different grid discretizations. Under the same boundary conditions and the same size of RZs, we found that the hyperfine and extremely refined grids produced almost identical results, including *V-J* curves, solute field, velocity field, and pressure field. Therefore, we use the hyperfine grid to acquire computational accuracy and to save computational resources. The average computational time for 2D and 3D simulations is 4.6 and 12.2 h, respectively on four parallel Intel® Xeon Gold 6248 CPUs of the High-Performance Computing Center (HPCC) of Nanjing University.

Notably, we first solve the steady-state flow field and then the transient solute field based on the coupled laminar flow model (steady-state) and the dilute matter transport model (transient-state). The flow and vortex structures within the fractures are steady when the solute passes through. To consider the influence of the solute transport distances, the different RZ shapes, and RZ sizes (RZs volume S_{ν}) on the solute transport process, three representative local flow fields located at the front, middle, and tail of 2D Fr-A and 3D Fr-A were selected as cases. The representative local flow fields include a complete RZ and its adjacent main flow zones, respectively, i.e., 2D RZ-A1, 2D RZ-A2, 2D RZ-A3 of 2D Fr-A and 3D RZ-A1, 3D RZ-A2, and 3D RZ-A3 of 3D Fr-A shown in Fig. 1. All results and discussions in the following are based on the selected local flow fields and RZs. Moreover, similar local flow fields were also chosen from the other four 2D fractures shown in Figs. S3–S6,

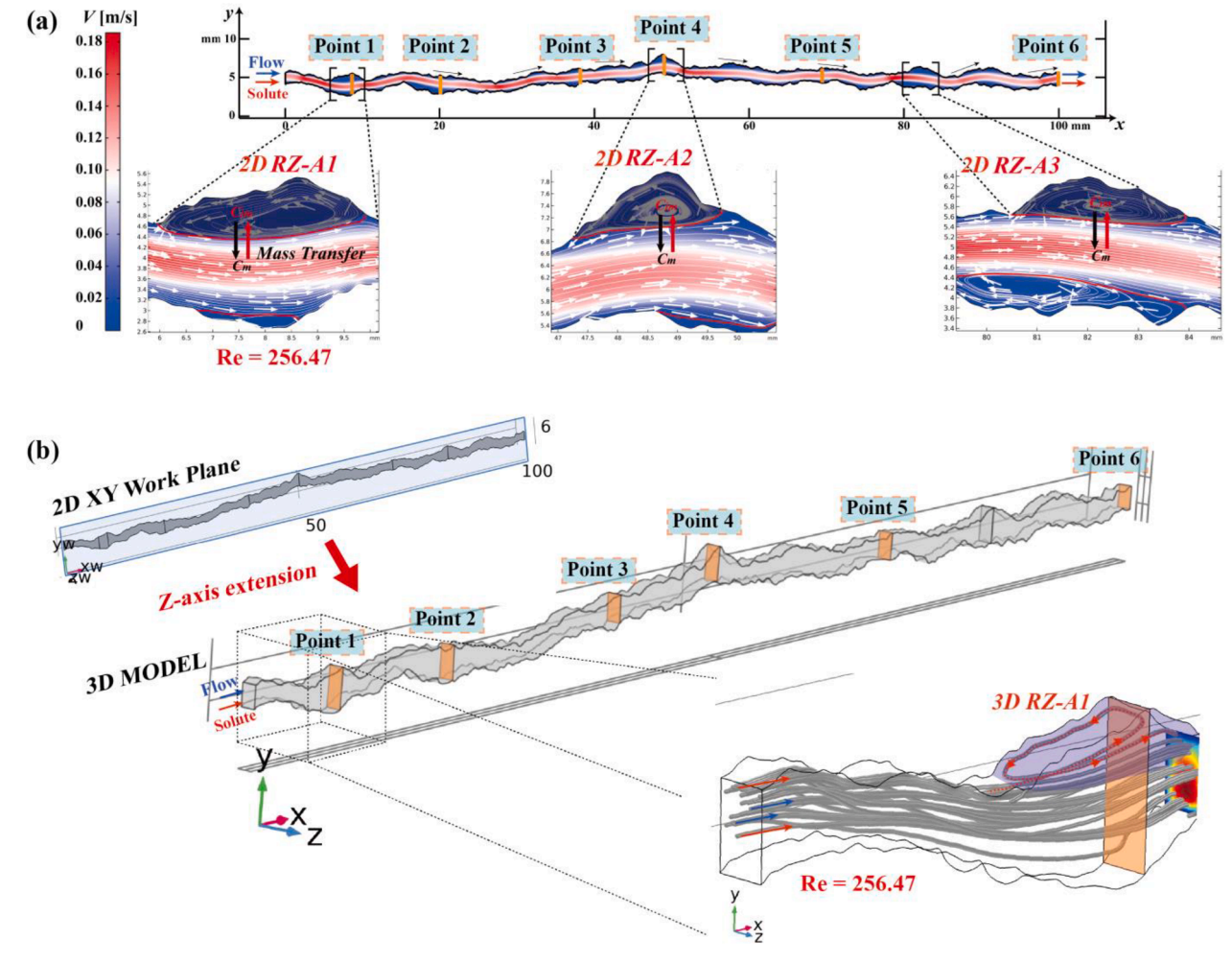


Fig. 1. (a) Location of six sampling points and three typical RZs in 2D Fr-A; (b) Establishment of the 3D physical model, 3D Fr-A.

which were used to verify the study results, extend more data, and fit mass transfer formulas.

2.2.3. Flow regime transition with increasing Reynolds number

To obtain a wide Re range, P_in was set to 20–400 Pa, and the corresponding hydraulic gradient was 0.02–0.4 to ensure sufficient fluid inertial effects (Re) for the evolution of RZs [39,40]. As Re increases, the flow regime transitions from Darcy flow to non-Darcy flow [41–45].

In this study, we employed the non-Darcy effect factor E [-] proposed by Zeng and Girgg [46] to characterize the flow regime transition from Darcy flow and non-Darcy flow:

$$E = \frac{b_1 V^2}{a_1 V + b_1 V^2} \tag{5}$$

where a_1 [s/m] and b_1 [s²/m²] are the viscous and the inertial coefficient of the Forchheimer equation $(J = a_1V + b_1V^2)$ [47], respectively. Fitting results of the Forchheimer equation in 2D and 3D rough single fractures are shown in Table S2.

(a)

7000

The critical value E=0.1, which indicates the pressure drop caused by inertial force accounts for 10 % of the total pressure drop, was used as an indicator to distinguish Darcy flow and non-Darcy flow [11,46,48]. Fig. S7 showed that the Forchheimer equation described the *V-J* curves well and the fitting coefficients (a_1 and b_1) are given in Table S2 which were used to determine E. The 1-E decreases with Re by more than 0.2 in both 2D and 3D Fr-A under the imposed pressure gradient (20 Pa < P_{L} in < 400 Pa), which indicates the flow regime transitions from Darcy flow to non-Darcy flow. Therefore, the range of Re for RZs' evolution is wide enough to include both Darcy and non-Darcy flow regimes and the flow regime transition with increasing Re is consistent with previous studies [11,12,41].

3. Results and discussion

250

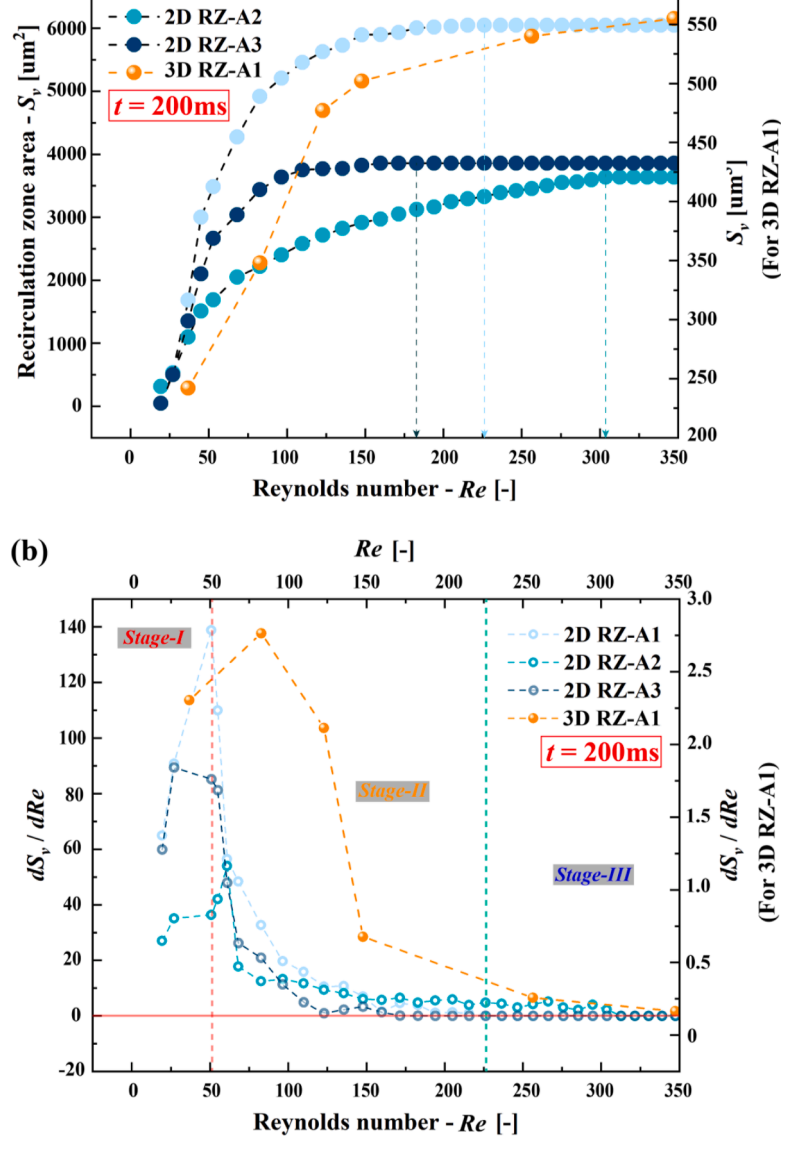
3.1. Evolution of RZs across the wide Re range

350

, 600

300

To investigate the full evolution process of RZs across a wide Re range, we quantify the RZs volume (S_v) as a function of Re because the



Re [-]

150

200

100

2D RZ-A1

Fig. 2. Evolution of the RZs volume under the wide range of flow regimes, S_v (a), and the growth rate of RZs volume, dS_v/dRe (b), with increasing Re.

varying S_{ν} with increasing Re is a fundamental feature reflecting the evolution of RZs [20,27,28]. A MATLAB®-based script identifies and measures the RZs volume (S_{ν}) in 2D and 3D rough single fractures [20, 30]. This script is based on the feature that the flow lines in the RZs are opposite to the flow lines in the MFZs. By setting the direction of the flow lines in the MFZs as the positive direction, the position and volume of the RZs can be determined according to the negative, integral flux. Fig. 2 (a) shows the evolution of S_{ν} with increasing Re. S_{ν} rises only up to a maximum value and then tends to flatten out due to the constraints imposed by the fixed void space and the MFZs. The evolution stages can therefore be seen as the different trends in the growth rate of S_{ν} with Re (dS_{ν}/dRe) .

Fig. 2(b) shows that the evolution of RZs across a wide Re range can be divided into three stages (the evolution process of 2D RZ-A1 is served as an example): (1) $Stage\ I$: Rapid growth stage, occurring mainly in the Re range from 0 to 50, where dS_V/dRe grows with Re, showing that S_V expands rapidly after initial formation in the flow field; (2) $Stage\ II$: Slow growth stage, occurring mainly in the Re range from 50 to 225, where dS_V/dRe starts to decrease until $dS_V/dRe = 0$; (3) $Stage\ III$: Fully developed stage, occurring in the range of Re > 225, where dS_V/dRe stabilizes at 0, indicating that the morphology of the RZs remains stable.

In addition, for different RZs at different positions of the same fracture or different fractures, their respective evolution stages also correspond to different Re range and S_v , which are induced by the geometric structure of the fracture wall surface, e.g., the angle between the fracture wall and the bulk flow direction (Moffatt, 1965). However, these minor differences in the Re ranges and S_v are negligible for the following discussion, because we focus on the specific solute transport process induced by the RZs at different evolution stages. Note that, compared to the 2D flow field (including fluid flow in the x and y directions (shown in Fig. 1(b))), the evolution process of RZs in 3D simulations was influenced by transverse flow (fluid flow in the z-direction). The Re ranges and S_v corresponding to different evolution stages are also different from 2D RZs.

3.2. Characterization of anomalous solute transport in rough single fractures

The flowing fluid induces the evolution of RZs, which in turn distinctly affects solute transport. A comprehensive view of the transport process associated with the 2D RZ-A1 and 3D RZ-A1 at successive time snapshots and for increasing *Re* is depicted in Figs. 3 and 4, respectively. Combined these two exemplary cases with the transport process associated with the 2D/3D RZ-A2 and 2D/3D RZ-A3 shown in Figs. S8–S11, which can be representative of all other RZs in all 2D and 3D fractures.

As shown in Figs. 3 and 4, the 2D RZ-A1 starts to form at *Stage I*. At this point, RZ just forms and S_{ν} is small, so that almost no solutes are trapped by it. Conversely, the solutes are mostly retained in a strip structure with a high concentration near the fracture wall surface. This phenomenon was first observed in 2D numerical simulations by Yeo [49].

Here we need to emphasize the difference between the RZs-MFZs interface and the solute "film". As Re continues to increase, the S_v increases rapidly. The evolution stage of RZs shifts from Stage I to Stage II. Meanwhile, the solute detained near the fracture wall disappeared due to the evolution of RZs. However, the solutes are also retained in strip structures around the interface between RZs and MFZs (RZs-MFZs interface), when solutes pass through the local flow field. Notably, in the following contents, the solutes detained around the RZs-MFZs interface are termed as the solute "film" (marked by blue lines in Fig. 3), which is the intermediate state of the solutes trapped by RZs in the flow field. The interface between RZs and MFZs is indeed a conceptual imaginary line (in both 2D and 3D cases) with 0 thickness. As mentioned in Section 3.1, the principle of the identification of RZs is based on the feature that the flow direction in the RZs is opposite to that of corresponding main flow channels (MFZs). The interface between RZs and MFZs is the point where the integral flux changes from positive to negative. However, the solute "film" is an actual strip with a certain thickness that holds solute around the interface between RZs and MFZs. For accurate identification and characterization of solute "film", please refer to Section 3.3.2.

Figs. 3 and 4 and Movies S1-S3 show that, when the solute plume

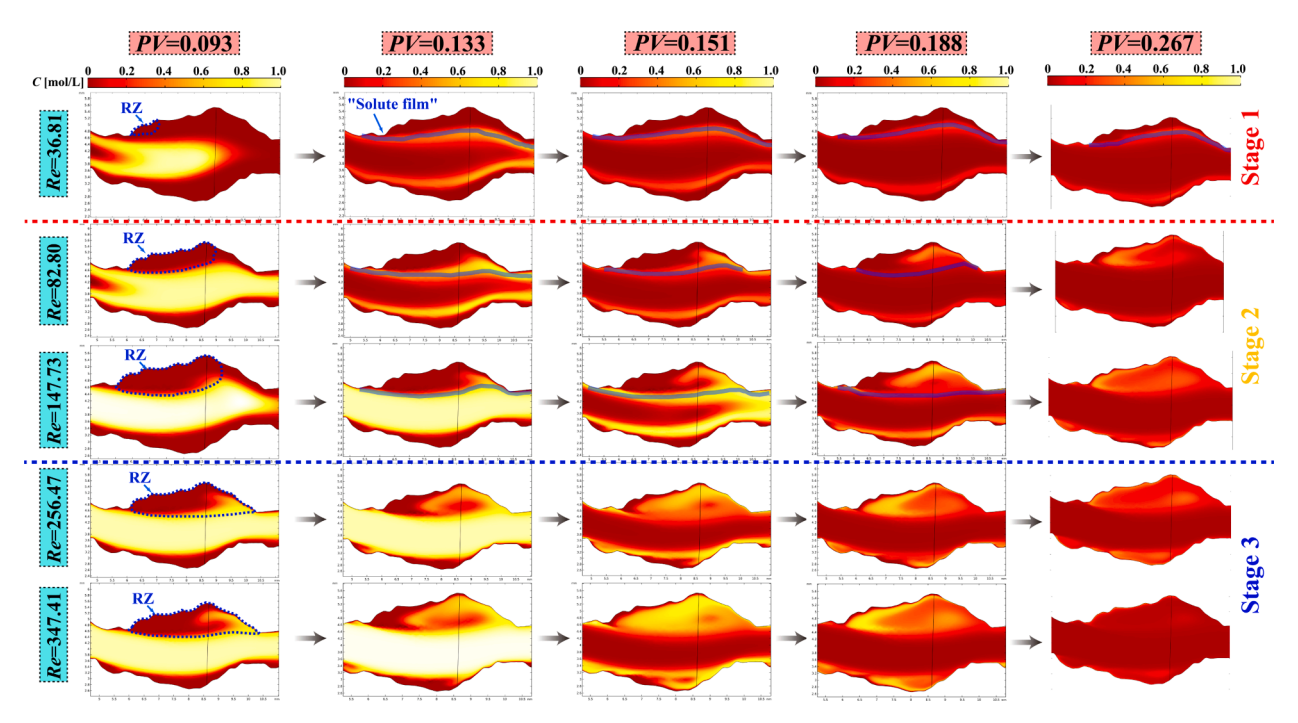


Fig. 3. Typical solute transport processes in a 2D recirculation zone (2D RZ-A1) within a fracture at successive pore volumes (PV = tq/A, q is the specific flux of fracture, and A is the fracture inlet area) and for the RZs formed across increasing Reynolds number (Re). Flow is from left to right. Solid lines with blue color indicate the solute "film" formed at the interface between the RZ and corresponding main flow channel (MFZ).

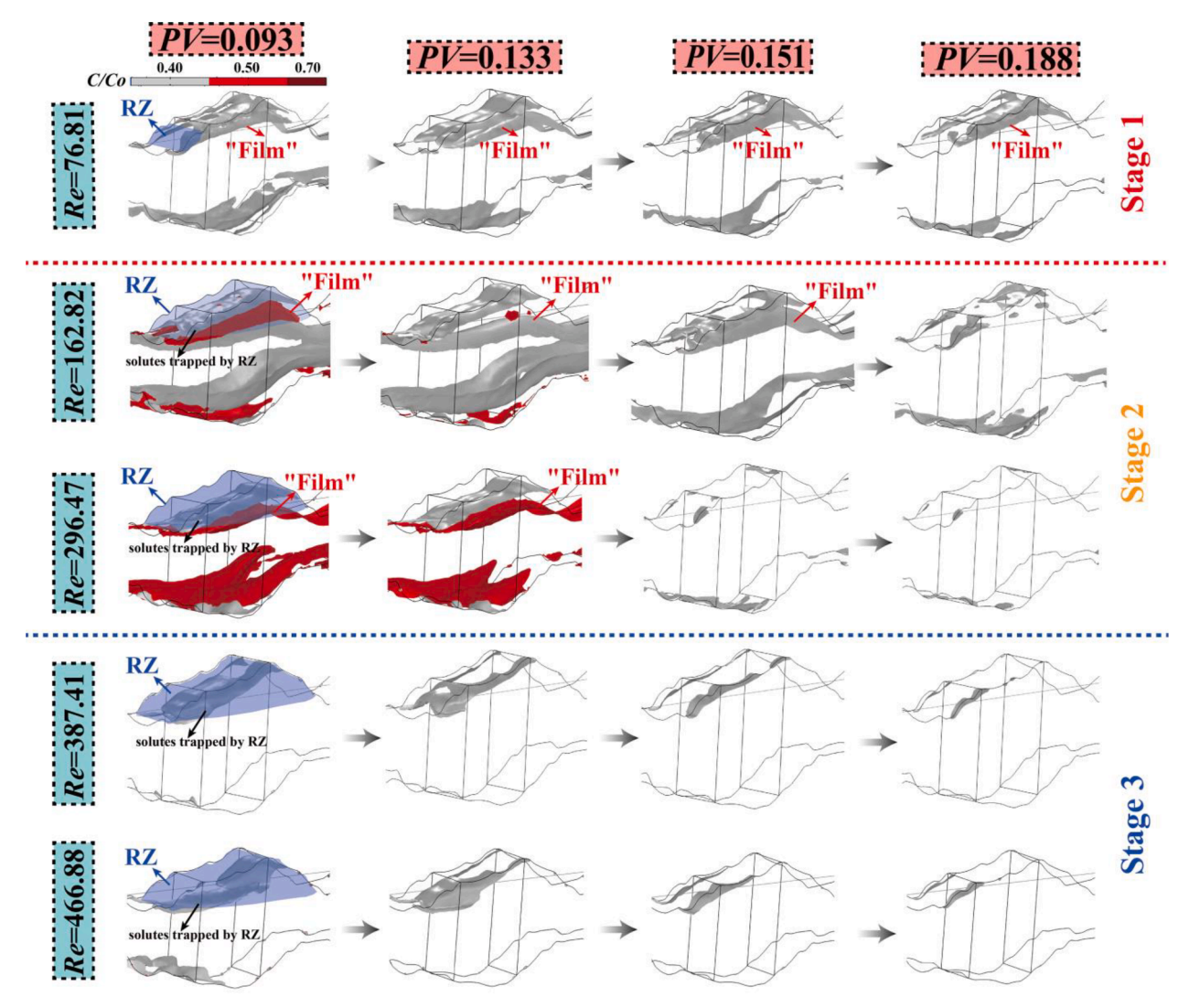


Fig. 4. Typical solute transport processes in a 3D recirculation zone (3D RZ-A1) within a fracture at successive pore volumes *PV* and for the RZs formed across increasing Reynolds number (Re). Flow is from left to right. Note that only the solute fields with concentration $C/C_0 \ge 0.4$ mol/L have been colored, the hollow areas are the area saturated with low solute concentration solute ($C/C_0 < 0.4$ mol/L). The solute "film" is represented by the strip with a certain concentration ($C/C_0 \ge 0.4$ mol/L) around the interface between RZs and MFZs or adjacent to the fracture wall surface. RZs are highlighted by the blue region.

front passed by the 2D/3D RZ-A1, some solutes were first trapped in the "film" then it has two migration pathways: (1) to enter the RZs, or (2) to continue to move along the MFZs. As shown in Movies S2–S5 once solutes enter RZs, they rotate around the RZ with the rotational flow and gradually spiral into the core of RZs.

Solute "film" was gradually dissipated by the above two migration pathways with time, until it completely disappeared, then the solutes trapped by RZs were released back into MFZs. As Re further increases, at $Stage\ III$, the solute "film" was not observed in the flow field at any time points. Therefore, when solute passes through RZs, it is directly trapped and then released by RZs. Moreover, as shown in Figs. S8–S11, regardless of the Re or the different evolution stages, the solute "film" at 2D/3D RZ-A2 and RZ-A3 was also not observed as the solute transport distance (L_s) increased.

To clearly describe the impact of evolving RZs in the microscale local flow field on the macroscale solute transport, we used BTCs of six sampling points from the fracture inlet to outlet (shown in Fig. 1) to characterize the macroscopic solute transport characteristic in fractures. The BTCs at sampling point 1 and point 6 under different Re of 2D Fr-A and 3D Fr-A are shown in Fig. 5. BTCs from other sampling points in 2D Fr-A and 3D Fr-A are shown in Figs. S12 and S13, and BTCs from the other four 2D fractures (2D Fr-B, 2D Fr-C, 2D Fr-D, and 2D Fr-E) are also

listed in Figs. S14–S17.

Under the influence of the evolving RZs, BTCs showed more complex anomalous solute transport phenomena. Firstly, the multi-modal peaks are observed in the BTCs at sampling point 1. Note that Fig. 5 only shows BTCs at points 1 and 6, which does not mean that multimodal BTCs are only found at point 1 near the fracture inlet. Multi-modal BTCs can also be observed at other sampling points or other parts of the fractures, e.g., BTCs at points 2 and 3 in 2D Fr-C and 2D Fr-B shown in Figs. S14 and S15. Secondly, the fluctuating tailings, that is, the tailings of BTCs, are strengthened and then shortened by the increasing Re. Thirdly, the above specific anomalous phenomena disappear with the increase of solute travel distance L_s (see inset Fig. 5(a') and (b')).

Here we employed quantitative indicators to measure the degree of macroscale anomalous transport. In this work, the parameter β [-] obtained by fitting the continuous time random walk (CTRW) model (see details in Text S4 and Fig. S18) and the second spatial moment (SSM) of BTCs were used as quantitative indicators. More explanations about the relationship between β , SSM, and the magnitude of the anomalous transport are given in Text S4, and the value of β , SSM in 2D Fr-A are shown in Table S3. The closer the β is to 2, the weaker anomalous transport is; the more significant anomalous transport corresponds to a larger SSM, and vice versa. The lines in the 2D x-z plane in Fig. 6

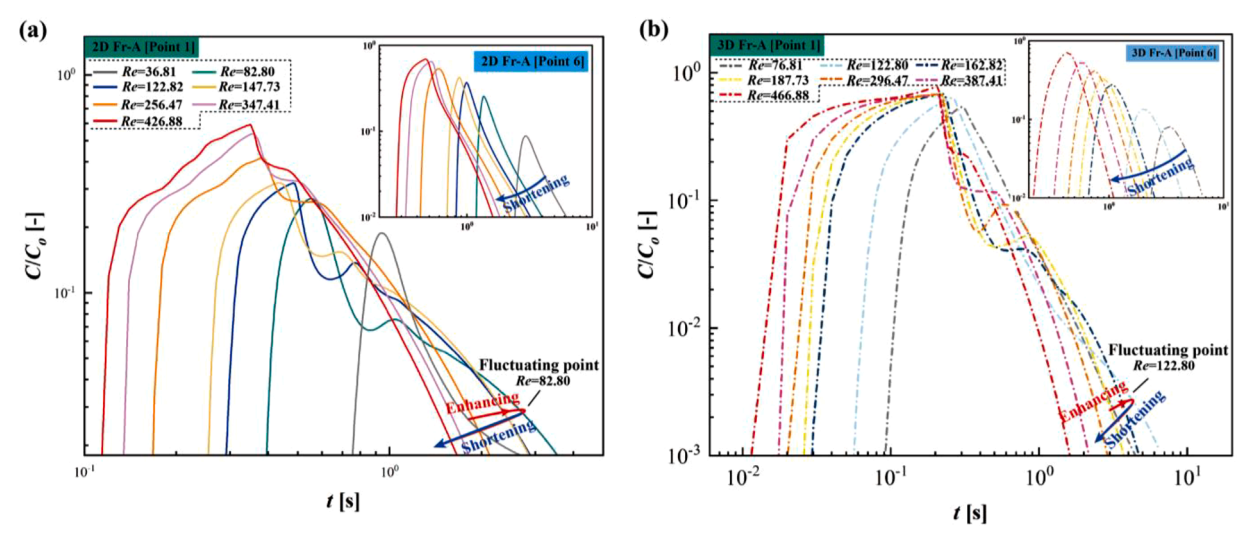


Fig. 5. BTCs observed in the sampling point 1 (a) and point 6 (a') of 2D Fr-A and sampling point 1 (b) and point 6 (b') of 3D Fr-A under the different Re.

represent the effect of Re on β and SSM at six sampling points. Note that the data used to obtain β (SSM) here are the concentration-time (C-t) data at different Re at different sampling points listed in Figs. S12 and S13. The fluctuating tailings and the multi-modal peaks at small L_s are parameterized to the nonmonotonicity of β and SSM with increasing Re, as shown in Fig. 6(a) and (c). Meanwhile, with the increase of solute travel distance L_s , β , and SSM obtained from the BTCs of sampling points 2–6 increase and decrease monotonically with Re, respectively, indicating that the anomalous effect is weakened with increasing L_s . Fig. 6 (b) and (d) illustrate the similar trends of BTCs in 3D Fr-A to those in 2D Fr-A. In the following sections, the phenomenon related to L_s is referred to as the transport length dependence. In addition, the functions between β , SSM, and Re of 2D Fr-B are also shown in Fig. A (Appendix C) to ensure the universality of the specific anomalous transport phenomena.

Moreover, it can be seen in Fig. 5 that the early arrival phenomenon strengthens monotonically with increasing *Re*, which indicates that the early arrival depends only on the *Re*. This is because the increased *Re* in MFZs leads to the solute remaining in the main channel breaking through quickly [18], while these solutes are not involved in the solute transport process related to the RZs. In this study, we focus on the role of recirculation zones on the solutes, so the early arrival is not further investigated here. Still, its contribution to other studies is also important, e.g., the anomalous transport prediction model [24,25,50].

3.3. Microscopic mechanism of macroscopic anomalous solute transport

3.3.1. Mass transfer between evolving RZs and main flow zones

As shown in Section 3.2, the evolution of RZs in microscale local flow fields significantly affects the solutes distribution and transport process in microscale local flow fields, which further determines the macroscale transport characteristics. Therefore, a comprehensive understanding of the microscale mass transfer process between RZs and MFZs is the basis for the mechanism investigation of anomalous transport phenomenon.

Notably, the validity of the physical parameterization of the mass transfer process between the RZs and MFZs in 2D rough single fractures has been verified by Zhou [30] and Zheng [51]. In this work, the mass transfer coefficient α [1/s] in the first order rate law was utilized to measure the mass transfer rate between the RZs and MFZs:

$$\alpha = \frac{(\partial C_{im}/\partial t)}{(C_{im} - C_m)} \tag{6}$$

where C_{im} [mol/L] is the average solute concentration inside the RZs; C_m [mol/L] is the average solute concentration in MFZs adjacent to the RZs. Note that when calculating α , both C_m and C_{im} do not include solutes

located at the RZs-MFZs interface, i.e., α quantified the direct mass transfer rate between RZs and MFZs, without considering the role of the solute "film". This is because the solute "film", as an intermediate state in the mass transfer process between RZs and MFZs, disappears in a relatively short period, and its impact on the mass transfer rate can be ignored. However, the solute "film" closely relates to the mechanism of anomalous transport phenomenon, which is mainly discussed in the following sections.

As shown in Fig. 7, α first fluctuated and then stabilized with the increasing PV, this is because both C_{im} and C_m vary with time. When the released solutes just reached the sampling point (small PV), the fluctuation of α with PV is attributed to the varying C_{im} and C_m with the instantaneous injection of solutes. As the solute plumes pass through the local flow field, some solutes are detained in the solute "film" but have not yet entered RZs where $C_{im}=0$ at the initial time. As PV increases, some of the solutes detained on the "film" enter the RZs (an increase in C_{im}), and other solutes pass through MFZs (a decrease in C_m). α starts to rise. α rises to its maximum at the time when solutes in MFZs have almost disappeared. However, as the solutes trapped by RZs are released into MFZs (C_{im} decreases, C_{m} increases), α begins to decrease. When C_{im} is equivalent to C_{m} , $\alpha=0$. However, the solute released in MFZs rapidly migrates downstream with the mainstream, causing $C_{im} > C_{mb}$ α increases again with PV. Finally, the above solute transport process continues but remains relatively stable, with α close to a constant, until the solutes trapped in RZs are completely consumed (i.e., $C_{im} = 0$). Therefore, similar to Zhou et al. (2019), only the constant α at this process where the solute release from RZs into MFZs accurately represents the magnitude of the mass transfer effect between RZs and MFZs, which is the α discussed in the main content.

Fig. 7(a)–(c) shows that the α increases with the increasing Re in 2D simulations. For 2D simulation, RZs and MFZs are two independent regions separated by the interface. The interface between RZ and MFZ is the zero-advection interface, where advection does not exist [30] and diffusion is the only way of the mass transfer process between RZs and MFZs. Only under pure molecular diffusion, α cannot increase with Re [30], but how does α increase with Re? Due to the RZs' evolution with Re, the rotational energy inside RZ increases with the increase of Re, which gradually transforms the transport within the 2D RZs from diffusion-dominated to advection-dominated [30]. Once the solutes diffused into the RZs, they rotated around the RZ with the rotational convection flow and spirals into the core of RZs, which increased the concentration gradient at the interface, thus leading to more mass exchange by diffusion per unit time, i.e., the increase of α , which is also proved by Zhou [30].

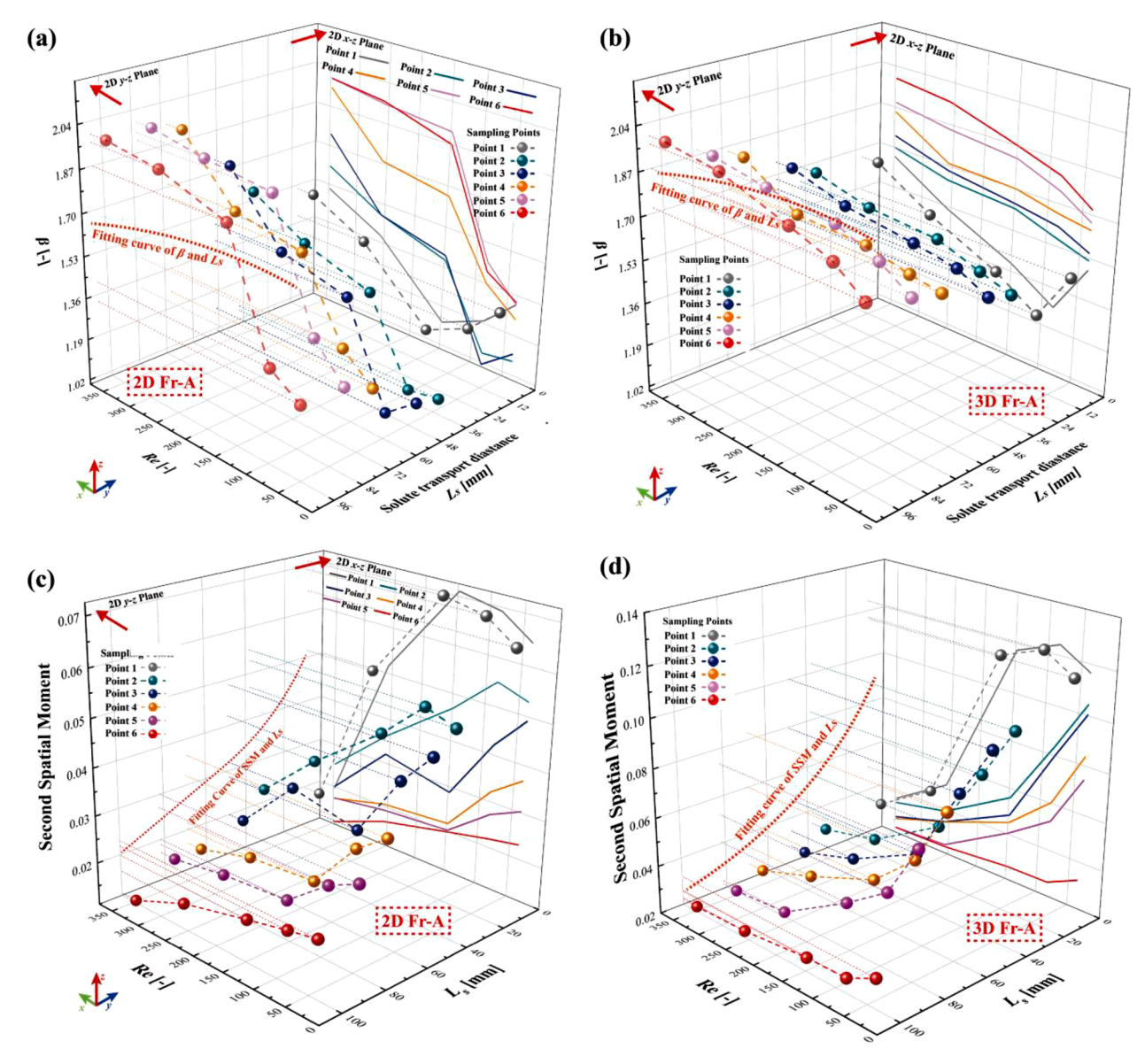


Fig. 6. The quantitative description of macroscale anomalous transport phenomena with increasing Re and solute transport distance (L_s). Evolution of parameter β with increasing Re and L_s in 2D Fr-A (a) and 3D Fr-A (b); Evolution of second spatial moment (SSM) with increasing Re and L_s in 2D Fr-A (c) and 3D Fr-A (d). The red fitting line in the 2D y-z plane is obtained by fitting the numerical relationship between the mean β (SSM) and L_s . Mean β (SSM) is framed based on the maximum/minimum β (SSM) value in the 2D y-z plane under the influence of Re at the same sampling point.

However, as Re continues to increase until RZs are fully developed, the transport within RZs becomes completely convection-dominated. Table 1 showed a significant increase in the Pelect number $(Pe_{im} = V_{im}d/D)$ within the RZs at Stages II and III $(Pe_{im} = 2 \times 10^3 - 2 \times 10^5)$ compared to Stage I $(Pe_{im} = 5 \times 10^2)$. Since α can be enhanced by convection flow within RZs, the significant difference in convective effect within RZs in different evolution stages may alter the corresponding mass transfer mode. To verify the above speculation, the relationships between Re_{rz} $(Re_{rz}$ represents the Re within RZs, defined as $\rho V_{im}d/\mu$, where V_{im} [m/s] is the average velocity inside RZs), mass transfer coefficient (α) and Sherwood number (Sh) are investigated by the mass transfer models that have been widely used to describe the different mode of heat and mass transfer process [51]:

$$\alpha = \alpha_o + a \operatorname{Re}_{rr}^b \tag{7}$$

$$Sh = Sh_o + mSc^{1/3}Re_{rz}^n$$
(8)

where a [-], b [-], m [-], and n [-] are dimensionless fitting

parameters, α_o [-] is the asymptotic mass transfer coefficient, Sh_o [-] is the asymptotic Sherwood number; Sc [-] is the Schmidt number defined as $\mu/\rho D$.

The Sherwood number (Sh) is a dimensionless version of the α that quantifies the relative importance of convective and diffusive mass transfer. In this work, Sh is calculated by $Sh = \alpha/(D/S^2)$ [30], and S [m] is the length of the RZs-MFZs interface. As mentioned in Section 2.2.2, the flow field is solved by a steady-state model, so S is a constant value when calculating Sh at each flow rate or Re.

Fig. 8(a) and (c) show that the power-law relation between α , Sh, and Re_{rz} in $Stage\ I$ of 2D simulations is similar to the power function observed by Zhou [30], indicating that the mass transfer mode between RZs and MFZs is diffusion-dominated. Because the mass transfer mode is ascribed to diffusion-dominated in Zhou's study [30]. However, Fig. 8 (b) and (d) show that the function between α , Sh, and Re_{rz} in $Stages\ II$ and III significantly differs from that in $Stage\ I$. Both α and Sh were characterized by a slowly rising regime at lower Re_{rz} followed by an asymptotic regime at higher Re_{rz} . This function trend indicates that, as

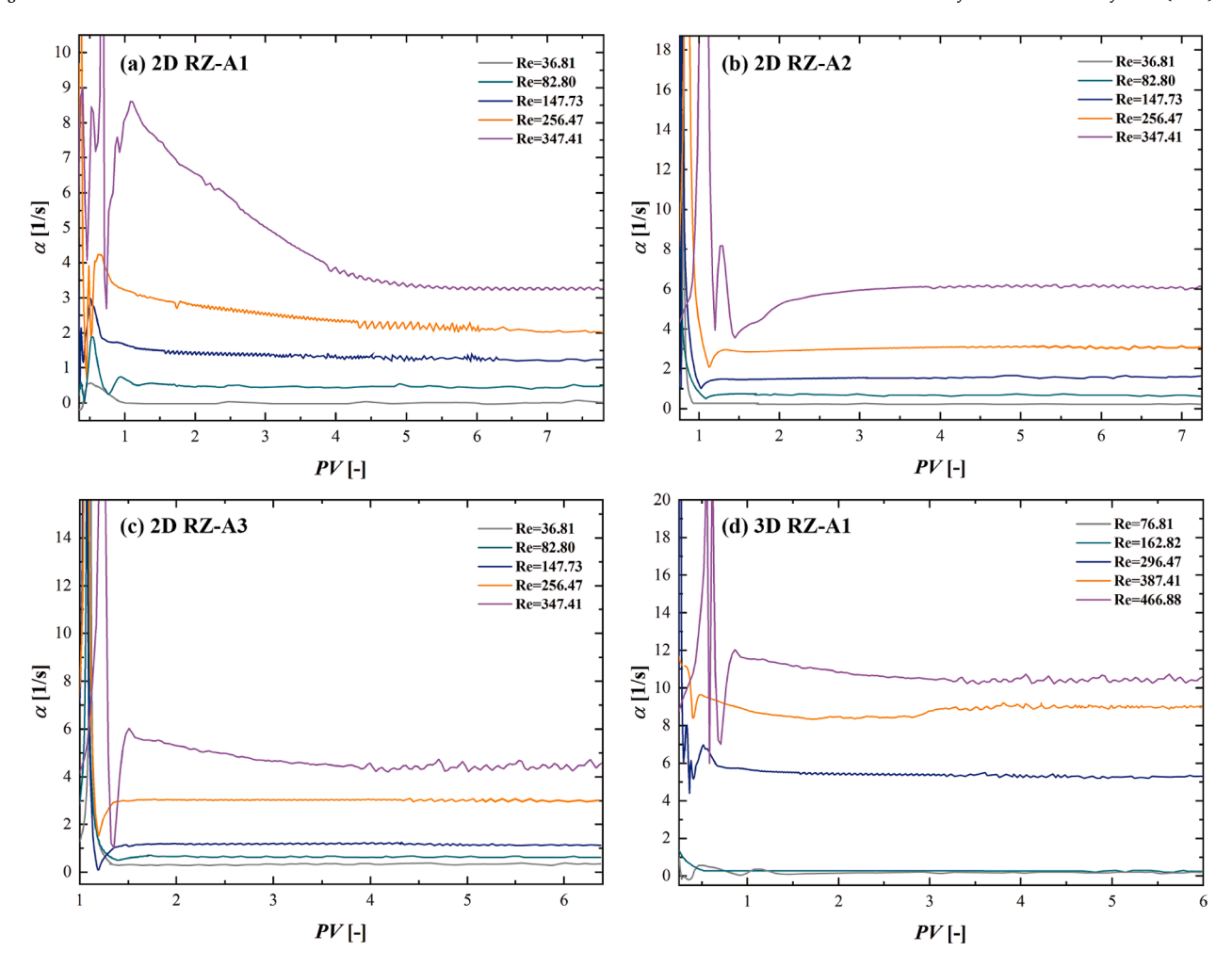


Fig. 7. Evolution of mass transfer coefficient α with pore volume (*PV*) between RZs and MFZs under different *Re.* (a) 2D RZ-A1; (b) 2D RZ-A2; (c) 2D RZ-A3; (d) 3D RZ-A1.

Table 1
Physical parameters of RZs (2D RZ-A1, 2D RZ-A2, and 2D RZ-A3), quantitative conditions for the solute "film" formation, and properties of solute "film" in 2D Fr-A.

No. of RZs	Ls/L [-]	P_in [Pa]	Re [-]	Stage	<i>Pe</i> _{im} [-]	<i>Pe_m</i> [-]	<i>Pe_{im}/Pe_m</i> [−]	f [-]	C _{MFCs} [-]	Film exist or not	Film thickness [mm]	Film concentration [mol/L]
2D RZ-	0.08	20	36.81	1	591.35	28,672.79	0.021	0.486	0.69	Yes	0.41	0.64
A1		50	82.8	2	2480.38	68,697.36	0.036	0.28	0.59	Yes	0.32	0.52
		100	147.73		5309.76	125,857.1	0.042	0.173	0.53	Yes	0.24	0.42
		200	256.47	3	17,836.47	221,400.7	0.081	0.157	0.39	No	_	_
		300	347.41		22,770.59	302,668.5	0.075	0.132	0.34	No	_	_
2D RZ-	0.48	20	36.81	1	661.32	30,452.2	0.022	0.441	0.41	No	_	
A2		50	82.8	2	3018.57	69,380.17	0.044	0.265	0.37	No	_	_
		100	147.73		5118.7	123,981.6	0.041	0.195	0.31	No	_	_
		200	256.47		7924.63	213,709.1	0.037	0.189	0.27	No	_	_
		300	347.41	3	10,252	287,387.1	0.036	0.177	0.25	No	_	_
2D RZ-	0.82	20	36.81	1	1345.33	25,010.35	0.054	0.576	0.36	No	_	
A3		50	82.8	2	5513.54	63,128.78	0.087	0.292	0.33	No	_	_
		100	147.73		11,269.52	124,573.9	0.090	0.162	0.35	No	_	_
		200	256.47	3	22,676.95	233,434.9	0.097	0.159	0.28	No	_	_
		300	347.41		32,353.54	322,709	0.100	0.123	0.24	No	_	-

Note: L_s/L [-] is the normalized solute transport distance, L [mm] is the fracture length; Pe_{lm} [-] is the Pelect number inside RZs, Pe_m [-] is the Pelect number inside MFZs; f [-] is the friction factor; $C_{MFZs} = C_m/C_o$ [-] is the normalized solute concentration inside MFZs.

RZs gradually evolve from $Stage\ II$ to $Stage\ III$, α continues to increase until it reaches the maximum value and then remains stable. The different α - Re_{rz} function trend of RZs at $Stages\ II$ and IIII from that of $Stage\ II$ indicates the shift of mass transfer mode from diffusion-dominated to "convection-dominated". The power indexes b and n in Eqs. (7) and (8), shown in Table S4, are critical indicators for

distinguishing the difference between diffusion-dominated and equivalent convection-dominated mass transfer. It should be noted that the so-called "convection-dominated" mass transfer in 2D simulation is due to significant enhancement in α induced by strong convection flow within RZs, the diffusion is still the only way for mass transfer process between MFZs and RZs in 2D simulations. In the following content, the

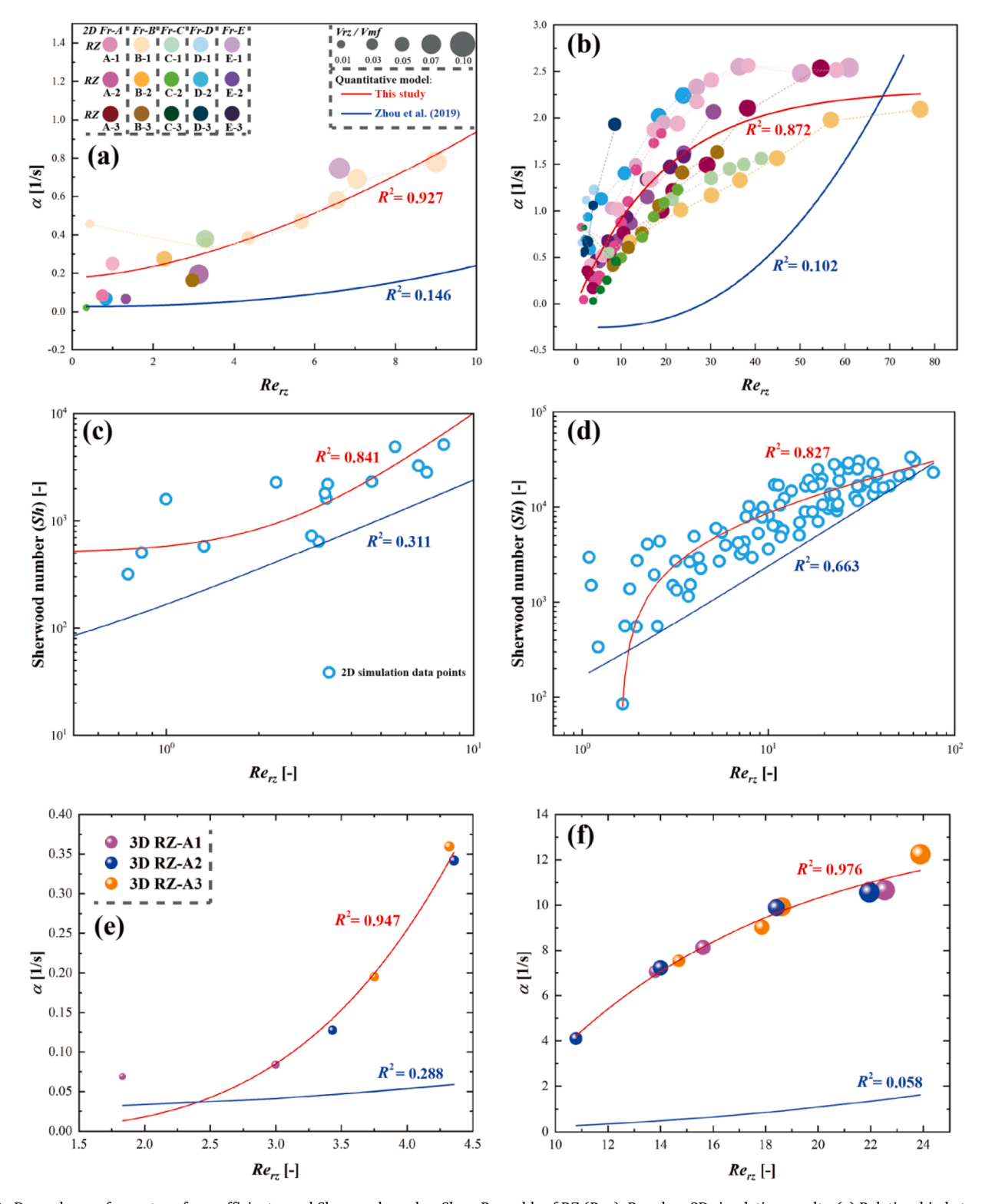


Fig. 8. Dependence of mass transfer coefficient α and Sherwood number Sh on Reynolds of RZ (Re_{rz}). Based on 2D simulation results: (a) Relationship between Re_{rz} and α for the rapidly growing RZs at $Stage\ I$ (dominated by diffusive mass transport); (b) relationship between Re_{rz} and α for near full or fully developed RZs at $Stage\ I$ and III (dominated by convective mass transfer); (c) relationship between Re_{rz} and Sh for the rapidly growing RZs at $Stage\ I$; (d) relationship between Re_{rz} and Sh for near full or fully developed RZs at $Stage\ I$ and III; Based on 3D simulation results: (e) Relationship between Re_{rz} and α for RZs at $Stage\ I$ and III.

altered mass transfer mode induced by completely convection-dominated transport within RZs in 2D simulations is referred to as the equivalent convection-dominated mass transfer.

Unlike 2D simulations, the increase in α of 3D simulations shown in Fig. 7(d) is due to direct convection flow between RZs and MFZs. As Re increases, the RZs-MFZs interface is no longer the zero-advection interface, where the direct advection flow exists [31]. As evinced by Fig. S19, for 3D RZ-A1 at $Stage\ I$, there are no direct flow lines and solute trajectories between RZs and MFZs, where the mass transfer mode is diffusion-dominated; for 3D RZ-A1 at $Stages\ II$ and III, there are direct flow lines and solute trajectories linked RZs and MFZs, which indicates the direct convection-dominated mass transfer. Interestingly, as shown in Fig. 8(e) and (f), the fitting results of Eq. (7) show a similar shift of the α - Re_{rz} trend as that of 2D simulations.

Therefore, for both 2D and 3D simulations, as Re increases, the mass transfer mode between the evolving RZs and MFZs shifts from diffusion-dominated to convection-dominated (or equivalent convection-dominated), leading to a significant increase in mass transfer rate (α). α of RZs at $Stages\ II$ and III (convection-dominated) increased by 5 times and 20 times compared to the α of RZs at $Stage\ I$ (diffusion-dominated) for 2D and 3D simulations, respectively.

The shift in the mass transfer mode between evolving RZs and MFZs from diffusion-dominated to convection-dominated implies a significant change in the microscale local transport process, which further determines the macroscale anomalous transport phenomenon observed in Section 3.2. Based on the comprehensive understanding of the mass transfer mode of evolving RZs in Section 3.3.1, the mechanisms of macroscale anomalous transport phenomenon are further investigated in the following sections.

3.3.2. Identification and the formation conditions of solute "film"

The proper identification of the solute "film" and "film" formation conditions is crucial in understanding the mechanisms underlying anomalous transport in fractures. The properties of the solute "film," namely its thickness and concentration, were recorded and listed in Table 1. The determination of concentration and thickness is achieved using direct measurements obtained from solute concentration distribution maps, as depicted in Fig. 3. The specific technique employed for these measurements is illustrated in Fig. S20. Note that, because of the instantaneous solute injection method, the solute "film" dissipates over time, leading to a decreased concentration and reduced thickness. The thickness and concentration of the solute "film" mentioned in Table 1 refer to its initial formation. Based on Table 1, we can establish the identifying criteria of the solute "film", i.e., the strip structures of solutes formed along the entire RZs-MFZs interface with a thickness greater than 14 % of the average fracture aperture (e_m) and a concentration greater than 12 % of the average concertation of RZ. For 2D Fr-A, the solute "film" is the strip structure with a thickness greater than 0.24 mm and a concentration greater than 0.4 mol/L. Note that although we chose three typical RZs in 2D Fr-A as examples to gain criteria for identifying the solute 'film', these criteria have been validated by other 2D and 3D fractures, shown in Figs. S8-S11).

After we succeeded in identifying the solute "film", we then investigated how the 'film' forms around the RZs-MFZs interface. Firstly, the solute "film" formed at the RZs-MFZs interface requires sufficient interfacial retention induced by the interfacial friction to trap solute particles. For both 2D and 3D simulations, previous studies have shown significant differences in flow velocity between RZs and MFZs [18–21, 30]. Due to the significant flow velocity difference (mainly in the flow direction) between RZs and MFZs at the interface, the flow resistance at the interface can be large enough for a stagnant zone formation (where the flow velocity is close to 0) as shown in Fig. S21. When the solute front in MFZs passes through the stagnation zone, some solutes are trapped and accumulated at the RZs-MFZs interface, forming a "film". We quantified the flow resistance of the RZs-MFZs interface using the friction factor f (the calculation method of f is listed in Text S5). Our

calculations showed that the "film" could form when f>0.173. In theory, a larger f suggests a greater difference in flow velocity at the interface of the RZs and MFZs, resulting in a more stable and thicker "film" structure. This finding is consistent with the results presented in Table 1

Furthermore, the establishment of suitable convective conditions between RZs and MFZs is crucial for the "film" formation. According to Table 1, f decreases with Re, indicating that the "film" structure becomes less stable. This is because the rotational energy in RZs increases with Re, which in turn induces the smaller velocity difference at the RZs-MFZs interface. Section 3.3.1 shows that, as RZs evolve with increasing Re, shifting the mass transfer mode from diffusion-dominated to convection-dominated significantly increases the mass transfer rate between RZs and MFZs. The enhanced mass transfer rate promotes the dissipation of solutes that should be detained around the RZs-MFZs interface, preventing solute accumulation and ultimately preventing "film" formation. Here we measured the magnitude of the convection effect between RZs and MFZs using Pe_{im}/Pe_m (where $Pe_m = V_m d/D$, V_m [–] is the average velocity in the corresponding MFZs of RZs). We found that the "film" could form when $Pe_{im}/Pe_m < 0.044$.

Moreover, enough solute concentration in MFZs (C_m) is also needed for "film" formation. If C_m is low (as in Fig. 3 where L_s is high), only a tiny amount of solute is detained at the RZs-MFZs interface, which is immediately dissipated by diffusion or advection. The solute cannot accumulate into a "film". Meanwhile, solute in MFZs is the solute source for maintaining relatively high concentrations of solute "film" (>12 % of the average concertation of RZ or > 0.4 mol/L for 2D-Fr-A), which is proved by the proportional relationship between "film" concentration and normalized solute concentration in MFZs C_{MFZs} ($C_{MFZs} = C_m/C_o$). Therefore, enough C_{MFZs} also determined the solute "film" formation. We found that the "film" could form when $C_{MFZs} > 0.5$. Since there is no "film" in the RZs near the fracture outlet (e.g., 2D RZ-A2 and 2D RZ-A3), the solute transport length dependency also affects solute "film" formation. However, the influence of transport length on "film" formation is included in that of enough solute concentration in MFZs. As shown in Fig. B (Appendix D), when solute reaches 2D RZ-A2, C_{MFZs} fall below 0.5, so the "film" cannot form. Additionally, C_{MFZs} is controlled by the fracture geometric properties. For example, the fracture wall roughness determines the quantity and size of RZs, which is positively correlated with the ability to retain solutes [20,29]. When the rougher fracture wall surface induces more RZs, these RZs would trap more solutes of MFZs and cause a significant decrease in C_{MFZ_S} in the flow field with larger L_S , and vice versa. As shown in Fig. B and Figs. S21-S22, at sampling point 3 $(L_s > 50)$ of 2D Fr-B and 2D Fr-C, although the solute transport distance is relatively large, the low roughness of the fracture wall (shown in Table S1) reserved enough C_{MFZs} for "film" formation ($C_{MFZs} > 0.5$). Therefore, the corresponding BTCs (Figs. S14 and S15) exhibit multi-modal and fluctuating tailings at relatively large Ls.

We therefore concluded formation conditions for the solute "film" in rough single fractures: (1) sufficient interfacial friction f > 0.173; (2) suitable convection between RZs and MFZs, $Pe_{im}/Pe_m < 0.044$; (3) enough solute concentration in MFZs, $C_{MFZs} > 0.5$.

3.3.3. Multi-modal peaks and tailing fluctuation of breakthrough curves

As shown in Fig. 3, the 2D RZ-A1 starts to form at Re = 36.81 (*Stage I*), and the solutes are mostly retained in a stratiform form with a high concentration near the fracture wall surface, and the corresponding BTCs do not show any multi-modal peaks at Re = 36.81. As Re continues to increase (36.81 < Re < 256.47), the S_V increases rapidly and the corresponding RZs evolve from $Stage\ I$ to $Stage\ II$. Meanwhile, the solute "film" starts to form at the RZs-MFZs interface, along with the multi-modal peaks of BTCs. As Re further increases ($Re \ge 256.47$, see 2D RZ-A1 in $Stage\ III$), at $Stage\ III$, the solute "film" was not observed in the flow field, and only the solutes captured by RZs were observed. The corresponding BTCs show the unimodal peak. Therefore, the multi-modal peaks of BTCs are closely related to the solute "film". The

solute "film" formation and its identification have been elucidated in Section 3.3.2. Here, we only focus on the solute "film" formed at the interface between 2D/3D RZ-A1 and MFZs, which determines the multimodal concentration peaks of BTCs.

The multiple peaks of BTCs indicate that after the solute front passes through sampling point 1 (i.e., the first concentration peak of BTCs), the concentration should have decreased with time. Still, the concentration has increased abnormally in a certain period. Fig. 9(a) shows that during PV = 0.133-0.188 (t = 690-1210 ms), the solute "film" has not been completely dissipated when some of its solutes trapped RZs. According to Fig. 9, as solute first flows toward point 1 (a1) to cause increased concentration, whereas it flows away from point 1 (a3) to cause decreased concentration. This explains the first main peak of BTCs. Meanwhile, some solutes are retained around the interface between RZs and MFZs, forming a certain thickness of solute "film". The solutes on the side near RZs are trapped and entered into RZs due to spin flow. The solutes entered into RZs and then rotated with RZs and its flow direction was changed to flow towards point 1 again, which coupled with residual solute "film", leading to the formation of the second concentration peak of BTCs. Moreover, due to the different geometric properties of the fracture wall surfaces and different sizes of RZs (RZs volume), the internal spin flow intensity also varies. If the spin flow inside RZs is sufficiently active, it induces the solutes on the solute "film" to repeatedly pass through the sampling points, forming more concentration peaks of BTCs, as shown in Figs. S15, S22 and S23. The same solute transport process is also confirmed by the 3D simulation in Fig. 9(b). When the solute "film" does not exist due to increasing Re, i.e., only the solutes trapped by RZs exist in the flow field, the multi-modal concentration peak disappears. Because the enhanced convective mass transfer between RZs and MFZs induces the solute trapped in RZs to quickly flow into the MFZs instead of continuing to rotate within RZs. Meanwhile, Figs. S22 and S23 are intended to demonstrate that the coexistence of solute "films" and solutes trapped by the RZs is the underlying mechanism for multiple concentration peaks, which is not only shown at sampling point 1.

According to the quantification of the mass transfer rate between RZs and MFZs in Section 3.3.1, if direct mass transfer exists between RZs and MFZs, the BTCs tailings should be monotonically shortened due to the increasing mass transfer rate with Re. However, the presence of solute "film" hinders the direct mass transfer between RZs and MFZs and alters the local solute transport process and the residence time of solutes in the flow field, which induces the fluctuating tailings of BTCs shown in Figs. 5 and 6. Combining with Figs. 3 and 4, it can be observed that, the coexistence of the solutes trapped by RZs and "film" induced heavier tailings than that under any of their separate effects, i.e., the heavier tailings of Re = 82.80-147.73 (*Stage II*) ($\beta = 1.12-1.20$) than that of Re= 36.81 (*Stage I*) (β = 1.32) and $Re \ge 256.47$ (*Stage III*) ($\beta > 1.39$). Because the solute is first trapped at the RZs-MFZs interface to form a "film", and then the solute on the "film" enters RZs or continues to migrate along MFZs. Due to the instantaneous injection method, the solutes on the "film" disappear after migrating through the above two pathways with time, and the solute entering RZs is released again. Therefore, the existence of solute "film" leads to a longer residence time or heavier tailings.

Note at Re = 36.81 (*Stage I*) where S_{ν} is very small, and almost no solutes are trapped by RZs. Only the "film" near the fracture wall surface mainly contributed to the tailing, which dissipates quickly along the MFZs. Therefore, the tailing at Re = 36.81 (*Stage I*) is weaker than that of Re = 82.80-147.73 (*Stage II*) where RZs and "film" coexist. At $Re \geq 256.47$ (*Stage III*), the "film" cannot be observed at the entire time scale due to the convection-dominated mass transfer process between RZs and MFZs. The enhanced convective mass transfer rate promotes the dissipation of solutes that should be trapped around the RZs-MFZs interface, preventing solute accumulation and thus preventing "film" formation. As a result, the solutes directly enter RZs and then are released by stronger convection flow, so the tailings at $Re \geq 256.47$ (*Stage III*) are

shorter than that of Re = 82.80-147.73 (Stage II).

Moreover, the tailings at $Re \ge 256.47$ (*Stage III*) are weaker than that of Re = 36.81 (Stage I). The disappearance of the "film" indicates that there is no intermediate state for solute detained in the flow field, and direct mass transfer occurs throughout the entire time scale. Because convection dominates the mass transfer mode under high Re conditions, the solute trapped in RZs was quickly released, resulting in weaker tailing under high Re conditions. Note that this finding does not contradict previous studies, which showed the development of RZs with Re leading to heavier tailings [19,21,26,28]. In previous studies, the evolution stages of RZs may be at Stage I due to the narrow hydraulic gradient or Re range, where the mass transfer model is diffusion-dominated. Thus the increase in S_{ν} leads to more trapped solutes and residence time. Meanwhile, the important role of solute "film" on the heavier tailings might be ignored, so the heavier tailings were only attributed to the development of RZs volume with increasing Re in previous studies.

3.3.4. Transport length dependence of anomalous transport

The transport length dependence in this study indicates the weak-ened anomalous phenomena with increasing L_s , e.g., the disappearance of multimodal BTCs, and the monotonically shortening tailings with the increasing Re. Combined with the important role of solute "film" in the multi-modal peaks and fluctuating tailings observed in Section 4.2.1, the transport length dependence of anomalous solute transport may be induced by the unformed solute "film" with increasing L_s .

As shown in Table 1 and Fig. 8, for different RZs, the different geometric properties of the fracture wall at which RZs are formed lead to inevitable differences in the size of S_{ν} , α , and f. However, by and large, the interfacial retention effect of the RZs-MFZs interface and mass transfer mode is not affected by L_s . As shown in Fig. B, as L_s increases, the normalized solute concentration in MFZs (C_{MFZs}) decreases as the solute front passes through the local flow field, this is because some solutes are trapped in the local flow field, resulting in a decrease in C_{MFZs} with increasing L_s, which is supported by Figs. S8-S11. Although the retention effect on the RZs-MFZs interface is not affected by L_s , even at the low Re with a strong interface retention effect (large f), there are little solutes were retained at the RZs-MFZs interface due to low C_{MFZs} . These little solutes were further quickly dissipated into RZs or MFZs (by diffusion into RZs or flowing along MFZs), leading to the inability of solute accumulation at the RZs-MFZs interface, so that the "film" is unable to form. At high Re condition (Stages II and III), strong convection (whether it is the convection inside RZs in 2D simulation or the direct convection flow between RZs and MFZs in 3D simulation) leads to fast solute dissipation at the RZs-MFZs interface, which made the "film" more difficult to form. Therefore, as L_s increases, the detained solutes do not need to go through an intermediate state, i.e., the "film", and a direct mass transport process has been established between RZs and MFZs by diffusion or convection. This leads to the disappearance of the multimodal peaks and the monotonic shortening of tailings with increasing *Re*, which can be explained by the increase of α with *Re* in Section 3.3.1.

In the above content, we have discussed the non-Fickian phenomenon and underlying mechanisms caused by the RZs and the formation of solute "film" under instantaneously injected solute conditions. One of the conditions for the solute "film" formation is sufficient C_{MFCs} (C_{MFCs} > 0.5), which is mentioned in Section 3.3.2. Therefore, for instantaneously injected solutes in the flow field, C_{MFCs} are relatively higher near the solute inlet, which is sufficient for the "film" formation. However, as the solute transport distance increases, the C_{MFCs} decrease due to convection, dispersion, or entry into RZs, resulting in the disappearance of solute "film" at a further distance from the outlet. This is the core content of this section.

Moreover, we further speculate that, for other scenarios with higher C_{MFCs} , i.e., continuously injected solute condition, the effects of RZs and solute "film" on solute transport may be more complex. As shown in previous literature using the continuously injected solute method [21,

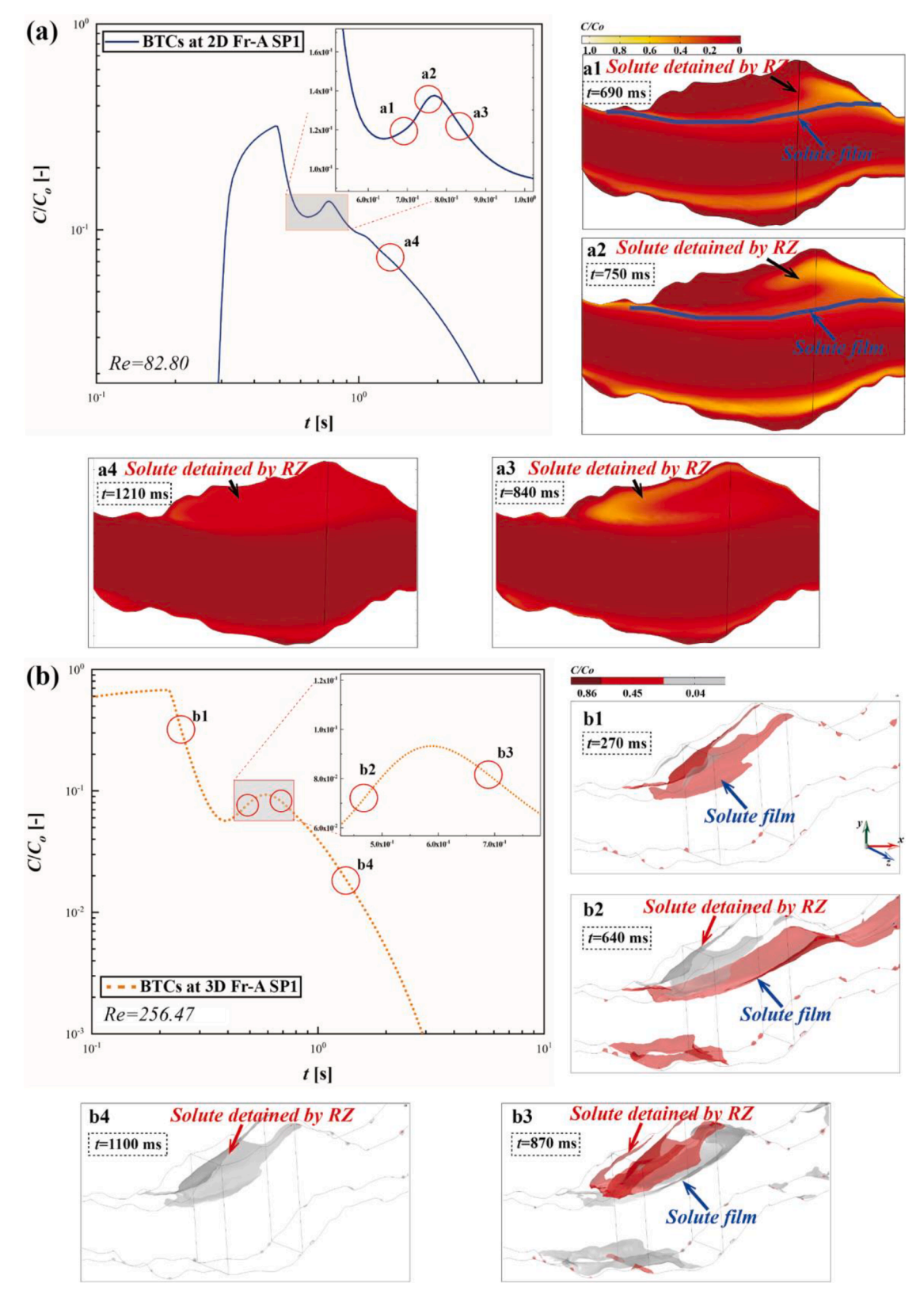


Fig. 9. Mechanism of multi-modal BTCs. (a) Solute superposition due to the interaction between RZs and solute "film" at the sampling point 1 (SP1) of 2D Fr-A under Re = 82.80 (*Stage II*); a1, a2, a3, and a4 represent the solute concentration distribution at 690 ms, 750 ms, 840 ms, and 1210 ms, respectively; (b) Solute superposition due to the interaction between RZs and solute "film" at the sampling point 1 of 3D Fr-A under Re = 256.47 (*Stage II*); b1, b2, b3, and b4 represent the solute concentration distribution at 270 ms, 640 ms, 870 ms, and 1100 ms respectively.

30], the normalized solute concentration at the sampling point (C) will become 1 ($C=C_{Sp}$ / C_{O} , C_{Sp} is the solute concentration at the sampling point) with increasing injection time. Meanwhile, the solute "film" will serve as a barrier to delay the entry of solutes into RZs until the concentration inside the RZ reaches 1, so the multimodal tailing phenomenon should be considered as the different time required for C to get 1. It can be also expected that, for the continuously-injected solutes condition, the concentration of the solute in MFCs (C_{MFCs}) will be significantly higher than that of instantaneously-injected solutes condition, and C_{MFCs} will approach 1 with increasing injection time. The higher C_{MFCs} are beneficial for the "film" formation at the location further away from the solute inlet. In the future, we will further investigate the non-Fickian solute transport induced by RZs and solute "film" under continuously injected conditions.

3.4. Impact of dimension on RZs evolution and associated anomalous transport

In this study, we set up both 2D and 3D physical models to consider the impact of dimensions on the RZs' evolution and their influence on anomalous transport. Although the results of 2D and 3D simulations shown in this study are similar, there are some differences caused by dimensions that need to be considered.

Firstly, the evolution of RZs was affected by the flow in the z-direction, i.e., the transverse flow. The transverse flow affects the volume growth of RZs in the z-direction and further affects the RZs' evolution. Therefore, the Re ranges corresponding to the evolution stages in 2D and 3D simulations are different, e.g., Stage I of 2D RZ-A1 corresponds to Re = 0-36.81, while Stage I of 3D RZ-A1 corresponds to Re = 0-76.81(Fig. 2). For different RZs, transverse flow may promote the evolution of RZs, which depends on the geometric properties of the fracture wall surface near RZs, and vice versa. Secondly, there are differences in the mass transfer mode shifts in the 2D and 3D flow fields. For 2D simulation, RZs and MFZs are two independent regions separated by the interface. The interface between RZ and MFZ is the zero-advection interface, where advection does not exist and diffusion is the only way for the mass transfer process between RZs and MFZs from Stage I to Stage II to Stage III. However, for 3D simulation, at Stage I, the mass transfer mode between 3D RZs and MFZs was the same as that of 2D simulation, i.e., RZs and MFZs are two independent regions separated by the interface which was diffusion-dominated. As RZs evolved from Stage I to Stage II, direct convective mass transfer is established between RZs and MFZs, that is, the mass transfer process between RZs and MFZs is directly driven by convection.

However, why the dimensionality does not seem to affect the threestage evolution RZs with increasing Re, as well as the corresponding shifts in the microscopic mass transfer mode, and thus the macroscopic anomalous transport phenomena in this study? Firstly, RZs' evolution is independent of dimensions. Because RZs should always go through a three-stage evolution with increasing Re due to the physical size limitations of the void space in which the RZs and MFZs formed. Meanwhile, the Re range we set is also sufficient for both 2D and 3D RZs to fully evolve in the fracture flow field. Secondly, although the mass transfer between 2D RZs and MFZs is dominated by diffusion, the enhanced convection flow due to the increasing Re inside 2D RZs enhances the mass transfer rate (α) of diffusion. In 3D simulations, the strong convection flow inside RZs directly connects MFZs, leading to the direct convective mass transfer, which also enhances α . The α at *Stages II* and III is 20 times higher than that at Stage I in 3D simulations due to convection-dominated mass transfer, while α at *Stages II* and *III* are also enhanced by 5 times due to the convection flow inside RZs in 2D simulations (Fig. 7). The increase in mass transfer rate leads to similar changes in solute distribution in microscopic local flow fields, e.g., the formation and dissipation of solute films, further leading to the similar macroscopic anomalous transport.

In addition, the expansion of the 3D model in the z-direction (1 mm)

in this study (Fig. 1) may limit the influence of transverse flow on the flow field and corresponding solute distribution. However, as mentioned above, the more significant transverse flow may not affect the three-stage evolution law of RZs due to the physical limitations on the RZs evolution, which in turn do not affect the corresponding law of microscopic mass transfer mode. The impact of dimensions can be further investigated based on more complex 3D physical models in future studies.

4. Conclusions

We investigated the effects of RZs on solute transport in rough single fractures across a wide Re range. The results show that the recirculation zones (RZs) undergo a three-stage evolution process with increasing Re, which is characterized by the growth rate of RZs volume (dS_V/dRe) : rapid growth stage ($Stage\ I$) where dS_V/dRe increases with Re, slow growth stage ($Stage\ II$) where dS_V/dRe decreases with Re, and fully developed stage ($Stage\ III$) where $dS_V/dRe = 0$.

The evolution of RZs has led to a shift in the mass transfer mode between RZs and MFZs at the microscale flow field, altering the solute transport process, which further leads to the more complex anomalous transport phenomenon. From Stage I to Stage II, the mass transfer mode between RZs and MFZs shifts from diffusion-dominated to convectiondominated, which significantly strengthens the mass transfer rate (α) between the RZs and MFZs. Along with the evolution of RZs, we found an interesting form of the detained solutes trapped by RZs, i.e., the solute "film" around the RZs-MFZs interface, due to the RZs-MFZs interface resistance. The solute "film" appears with the evolution of RZs at Stage I and then disappears at Stage III. During Stage II, the coexistence between the solutes trapped by the RZs and the solute "film" induced the multi-modal concentration peaks, prolonged the solute residence time, and thus strengthened the tailings of BTCs. From Stage II to Stage III, the "film" disappears due to the weakening of RZs-MFZs interface resistance and the rapid dissipation of solutes accumulated at the RZs-MFZs interface by convection. The formation and disappearance of solute "film" strengthen and shorten the solute residence time in the flow field, respectively, which explains the fluctuating tailings with increasing Re. In addition, the increase in solute transport distance L_s leads to a decrease in solute concentration in MFZs, which also prevents the formation of solute "film" at the RZs-MFZs interface. Therefore, as L_s increases, the multi-modal BTCs disappear and the tailing monotonically weakens with the increase of Re due to increasing α .

The full evolution process of the RZs across a wide *Re* range and associated impacts on the microscopic mass transfer process in fractures are first investigated in this study, which deepens our understanding of anomalous transport in fractured media. This study also provides favorable evidence of the convective mass transfer mode for establishing the solute transport models over a wide *Re* range in the future.

CRediT authorship contribution statement

Kun Xing: Writing – original draft, Software, Methodology, Investigation, Formal analysis, Conceptualization. Xiaoqing Shi: Writing – review & editing, Supervision, Funding acquisition, Conceptualization. Peter K. Kang: Writing – review & editing, Validation, Methodology. Xueyuan Kang: Writing – review & editing, Validation, Funding acquisition. Jiazhong Qian: Validation, Resources. Lei Ma: Validation, Resources. Jichun Wu: Writing – review & editing, Resources.

Declaration of competing interest

The authors declare that they have no known competing financial interests or personal relationships that could have appeared to influence the work reported in this paper.

Data availability

Data will be made available on request.

Acknowledgments

This work was supported by the Special fund for Carbon Peak and Carbon Neutrality Science and Technology Innovation of Jiangsu

Province in 2022 (BE2022603) and the National Natural Science Foundation of China (42202267 and 41977157). Peter K. Kang acknowledges the support by the National Science Foundation under Grant no. EAR-2046015. Xueyuan Kang acknowledges the support by the China Postdoctoral Science Foundation (2022M711565) and Jiangsu Funding Program for Excellent Postdoctoral Talent (20220ZB15). We are also grateful to the High-Performance Computing Center (HPCC) of Nanjing University for doing numerical calculations using its blade cluster system.

Supplementary materials

Supplementary material associated with this article can be found, in the online version, at doi:10.1016/j.ijheatmasstransfer.2024.125292.

Appendix A

Parameters used in numerical simulations for fluid flow.

Parameters and methods	Specific settings				
Flow State	Single phase; Steady-state				
Global definition	P_in [Pa]				
Geometry	Unit: mm				
Material	Incompressible Newtonian fluid: Water				
Governing equation	Navier-Stokes equation (NSE)				
Fracture wall surface	No slip; Wall movement: Zero				
The inlet of fracture flow	Dirichlet boundary; Initial value: P_in				
The outlet of fracture flow	Dirichlet boundary; Initial value: Defaulted (0 Pa)				
Grid settings	Hyperfine hydrodynamics control grids				
Solver configuration	Steady-state algebraic multigrid solver (spf)				

Appendix B

Parameters used in numerical simulations for solute transport.

Parameters and methods	Specific settings				
Flow State	Single phase; Time-dependent				
Global definition	C_o [mol/L]				
Geometry	Unit: mm				
Material	Solute: Sodium Chloride (NaCl)				
Governing equation	Advection-dispersion equation (ADE)				
Fracture wall surface	No slip; No flux; Wall movement: Zero				
The inlet of solute concentration	Dirichlet boundary;				
	Initial value: Co (1 mol/L); Instantaneous injection				
The outlet of solute concentration	Open boundary condition;				
	Initial value: C (0 mol/L)				
Grid settings	Hyperfine hydrodynamics control grids				
Solver configuration	Time-dependent segregated solver				

Appendix C

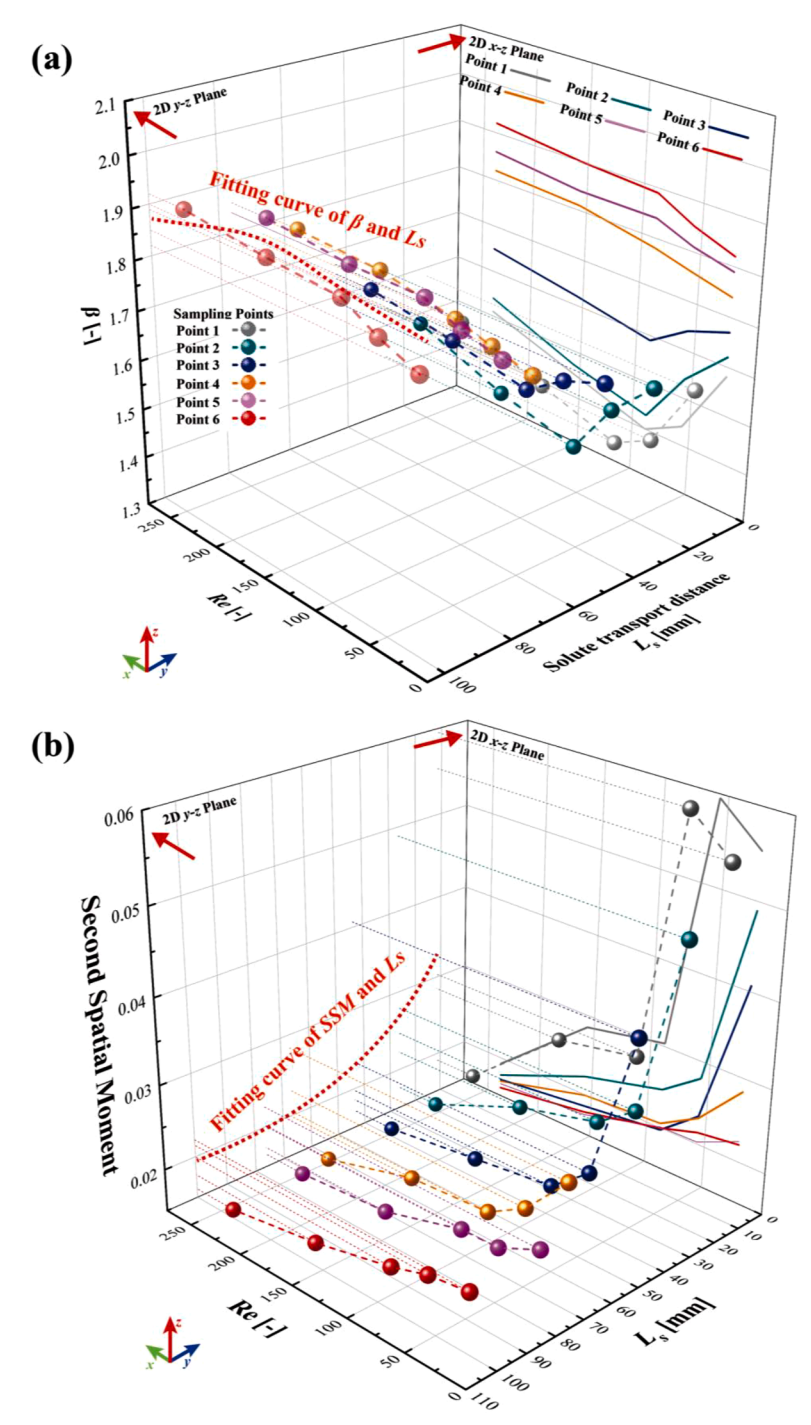


Fig. A. Evolution of parameter β (a) and second spatial moment (SSM) (b) with Re and L_s in 2D Fr-B.

Appendix D

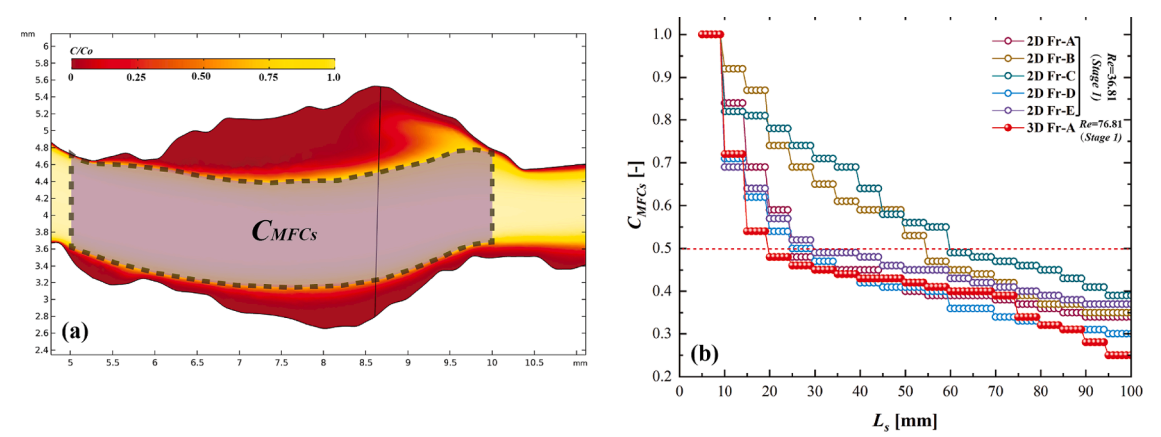


Fig. B. (a) Diagrammatic sketch of the normalized solute concentration in MFZs (C_{MFZs}); (b) Evolution of C_{MFZs} with increasing solute transport distance L_{s} .

References

- B. Berkowitz, Characterizing flow and transport in fractured geological media: a review, Adv. Water Resour. 25 (8/12) (2002) 861–884.
- [2] Y.F. Chen, J.Q. Zhou, S.H. Hu, R. Hu, C.B. Zhou, Evaluation of Forchheimer equation coefficients for non-Darcy flow in deformable rough-walled fractures, J. Hydrol. 529 (2015) 993–1006.
- [3] A.P. Oron, B. Berkowitz, Flow in rock fractures: the local cubic law assumption reexamined, Water Resour. Res. 34 (11) (1998) 2811–2825.
- [4] M. Ferer, D. Crandall, G. Ahmadi, D.H. Smith, Two-phase flow in a rough fracture: experiment and modeling, Phys. Rev. E 84 (1) (2011) 016316.
- [5] M. Klepikova, Y. Méheust, C. Roques, N. Linde, Heat transport by flow through rough rock fractures: a numerical investigation, Adv. Water Resour. 156 (2021) 100022.
- [6] T.A. Appuhamillage, V.A. Bokil, E. Thomann, E. Waymire, B.D. Wood, Solute transport across an interface: a Fickian theory for skewness in breakthrough curves, Water Resour. Res. 46 (2010) W07511.
- [7] J.H. Cushman, T.R. Ginn, Fractional advection-dispersion equation: a classical mass balance with convolution-Fickian flux, Water Resour. Res. 36 (2000) 3763.
- [8] M. Dentz, T.L. Borgne, A. Englert, B. Bijeljic, Mixing, spreading and reaction in heterogeneous media: a brief review, J. Contam. Hydrol. 120–121 (0) (2011) 1–17.
- [9] X. Sanchez-Vila, D. Femandez-Garcia, A. Guadagnini, Interpretation of column experiments of transport of solutes undergoing an irreversible bimolecular reaction using a continuum approximation, Water Resour. Res. 46 (12) (2010) W12510.
- [10] G.M. Porta, S. Chaynikov, J.F. Thovert, M. Riva, A. Guadagnini, P.M. Adler, Numerical investigation of pore and continuum scale formulations of bimolecular reactive transport in porous media, Adv. Water Resour. 62 (pt.B) (2013) 243–253.
- [11] R.W. Zimmerman, A. Al-Yaarubi, C.P. Chris, C.A. Grattoni, Non-linear regimes of fluid flow in rock fractures, Int. J. Rock Mech. Min. Sci. 41 (3) (2004) 1–7.
- [12] J.Z. Qian, Z. Chen, H.B. Zhan, S.H. Luo, Solute transport in a filled single fracture under non-Darcian flow, Int. J. Rock Mech. Min. Sci. 48 (1) (2011) 132–140.
- [13] L.C. Wang, M.B. Cardenas, Transition from non-Fickian to Fickian longitudinal transport through 3-D rough fractures: scale-(in)sensitivity and roughness dependence, J. Contam. Hydrol. 198 (Mar) (2017) 1–10.
- [14] L.C. Wang, M.B. Cardenas, W. Deng, P.C. Bennett, Theory for dynamic longitudinal dispersion in fractures and rivers with Poiseuille flow, Geophys. Res. Lett. 39 (5) (2012) 131–138.
- [15] A. Fiori, 2 Channeling, channel density and mass recovery in aquifer transport, with application to the MADE experiment, Water Resour. Res. 50 (12) (2014) 9148–9161.
- [16] P.K. Kang, S. Brown, R. Juanes, Emergence of anomalous transport in stressed rough fractures. Earth Planet. Sci. Lett. 454 (2016) 46–54.
- [17] P.K. Kang, J.D. Hyman, W.S. Han, M. Dentz, Anomalous transport in threedimensional discrete fracture networks: interplay between aperture heterogeneity and injection modes, Water Resour. Res. 56 (11) (2020) 1–22.
- [18] D. Bolster, Y. Meheust, T.L. Borgne, J. Bouquain, P. Davy, Modeling preasymptotic transport in flows with significant inertial and trapping effects—The importance of velocity correlations and a spatial Markov model, Adv. Water Resour. 70 (Aug) (2014) 89–103.
- [19] M.B. Cardenas, D.T. Slottke, R.A. Ketcham, J.M. Sharp, Navier–Stokes flow and transport simulations using real fractures shows heavy tailing due to eddies, Geophys. Res. Lett. 34 (14) (2007) 176–192.
- [20] L.C. Wang, M.B. Cardenas, J.Q. Zhou, R.A. Ketcham, The complexity of nonlinear flow and non-Fickian transport in fractures driven by three-dimensional recirculation zones, J. Geophys. Res. 125 (9) (2020) 1–14.

- [21] Z. Dou, Z. Chen, Z.F. Zhou, J. Wang, Y. Huang, Influence of eddies on conservative solute transport through a 2D single self-affine fracture, Int. J. Heat Mass Transf. 121 (Jun) (2018) 597–606.
- [22] H. Moffatt, Viscous eddies near a sharp corner, J. Fluid Mech. 18 (1965) 217–224.
- [23] J.Z. Qian, L. Min, Z. Chen, H.B. Zhan, Eddy correlations for water flow in a single fracture with abruptly changing aperture, Hydrol. Process. 26 (2012) 3369–3377.
- [24] L. Sun, J. Niu, F. Huang, J.C. Feng, C.H. Wu, H. Qiu, B.X. Hu, An efficient fractional-in-time transient storage model for simulating the multi-peaked breakthrough curves, J. Hydrol. 600 (2021) 126570.
- [25] M. Yin, R. Ma Y. Zhang, S. Wei, G.R. Tick, J.Q. Wang, Z.Y. Sun, H.G. Sun, C. M. Zheng, A distributed-order time fractional derivative model for simulating bimodal sub-diffusion in heterogeneous media, J. Hydrol. 591 (2020) 125504.
- [26] M.B. Cardenas, D.T. Slottke, R.A. Ketcham, J.M. Sharp, Effects of inertia and directionality on flow and transport in a rough asymmetric fracture, J. Geophys. Res. 114 (2009) B06204.
- [27] S. Briggs, B.W. Karney, B.E. Sleep, Numerical modeling of the effects of roughness on flow and eddy formation in fractures, J. Rock Mech. Geotech. Eng. 9 (1) (2017) 105–115.
- [28] J.Q. Zhou, L.C. Wang, C.D. Li, H.M. Tang, L.P. Wang, Effect of fluid slippage on eddy growth and non-Darcian flow in rock fractures, J. Hydrol. 581 (2020) 124440.
- [29] J.Q. Zhou, C.D. Li, L.C. Wang, H.M. Tang, M. Zhang, Effect of slippery boundary on solute transport in rough-walled rock fractures under different flow regimes, J. Hydrol. 598 (2021) 126456.
- [30] J.Q. Zhou, L.C. Wang, Y.F. Chen, M.B. Cardenas, Mass transfer between recirculation and main flow zones: is physically based parameterization possible? Water Resour. Res. 55 (1) (2019) 345–362.
- [31] S.H. Lee, I.W. Yeo, K.K. Lee, R.L. Detwiler, Tail shortening with developing eddies
- in a rough-walled rock fracture, Geophys. Res. Lett. 42 (15) (2015) 6340–6347. [32] L. Guarracino, D. Jougnot, A fractal model for effective excess charge density in variably saturated fractured rocks, J. Geophys. Res. 127 (3) (2022) 022982.
- [33] Y. Jin, J. Dong, X. Zhang, X. Li, Y. Wu, Scale and size effects on fluid flow through self-affine rough fractures, Int. J. Heat Mass Transf. 105 (2017) 443–451.
- [34] J.T. Zhu, Y.Y. Chen, Effective permeability of fractal fracture rocks: significance of turbulent flow and fractal scaling, Int. J. Heat Mass Transf. 116 (2018) 549–556.
- [35] M. Madadi, C.D. VanSiclen, M. Sahimi, Fluid flow and conduction in twodimensional fractures with rough, self-affine surfaces: a comparative study, J. Geophys. Res. 108 (B8) (2003) 1–10.
- [36] A.M. Tartakovsky, P. Meakin, Simulation of unsaturated flow in complex fractures using smoothed particle hydrodynamics, Vadose Zone J. 4 (3) (2005) 848–855.
- [37] K. Develi, T. Babadagli, Experimental and visual analysis of single-phase flow through rough fracture replicas, Int. J. Rock Mech. Min. Sci. 73 (2015) 139–155.
- [38] S.R. Ogilvie, E. Isakov, P.W.J. Glover, Fluid flow through rough fractures in rocks. II: a new matching model for rough rock fractures, Earth and Planet Sci. Lett. 241 (3–4) (2006) 454–465.
- [39] R. Liu, B. Li, Y. Jiang, Critical hydraulic gradient for nonlinear flow through rock fracture networks: the roles of aperture, surface roughness, and number of intersections, Adv. Water Resour. 88 (Feb) (2016) 53–65.
- [40] L.C. Wang, M.B. Cardenas, T.J. Wang, J.Q. Zhou, L.Z. Zheng, Y.F. Chen, X. Chen, The effect of permeability on Darcy-to-Forchheimer flow transition, J. Hydrol. 610 (2022) 127836.
- [41] P.Y. Guo, M. Wang, M.C. He, Y.W. Wang, K. Gao, W.L. Gong, Experimental investigation on macroscopic behavior and microfluidic field of nonlinear flow in rough-walled artificial fracture models, Adv. Water Resour. 142 (2020) 103637.
- [42] J.S. Konzuk, B.H. Kueper, Evaluation of cubic law based models describing single phase flow through a rough-walled fracture, Water Resour. Res. 40 (2) (2004) 1–17.

- [43] T.W. Schrauf, D.D. Evans, Laboratory studies of gas flow through a single natural fracture, Water Resour. Res. 22 (7) (1986) 1038–1050.
- [44] Y. Luo, Z. Zhang, Y. Wang, J. Nemcik, J. Wang, On fluid flow regime transition in rough rock fractures: insights from experiment and fluid dynamic computation, J. Hydrol. 607 (2022) 127558.
- [45] Z. Zhang, J. Nemcik, Fluid flow regimes and nonlinear flow characteristics in deformable rock fractures, J. Hydrol. 477 (1) (2013) 139–151.
- [46] Z. Zeng, R. Grigg, A criterion for non-Darcy flow in porous media, Transp. Porous Media 63 (1) (2006) 57–69.
- [47] P. Forchheimer, Wasserbewegung durch boden, Z. Vereins Deutscher Ingenieure 45 (50) (1901) 1782–1788.
- [48] M. Javadi, M. Sharifzadeh, K. Shahriar, Y. Mitani, Critical Reynolds number for nonlinear flow through rough-walled fractures: the role of shear processes, Water Resour. Res. 50 (2) (2014) 1789–1804.
- [49] I.W. Yeo, Effect of fracture roughness on solute transport, Geosci. J. 5 (2) (2001) 145–151.
- [50] A. Cortis, B. Berkowitz, Computing "anomalous" contaminant transport in porous media: the CTRW MATLAB toolbox, Ground Water 43 (6) (2005) 947–950.
- [51] L.Z. Zheng, L.C. Wang, T.J. Wang, Z.L. Wang, X. Chen, Mass transfer between recirculation zone and main flow domain in fractures: is the first order rate law valid? J. Hydrol. (2022) 128352.